The Formation of Small-Scale Atmospheric Vortices via Horizontal Shearing Instability

MICHAEL S. BUBAN

Cooperative Institute for Mesoscale Meteorological Studies, University of Oklahoma, and NOAA/OAR/National Severe Storms Laboratory, Norman, Oklahoma

CONRAD L. ZIEGLER

NOAA/National Severe Storms Laboratory, Norman, Oklahoma

(Manuscript received 10 December 2014, in final form 25 September 2015)

ABSTRACT

Motivated by high-resolution observations of small-scale atmospheric vortices along near-surface boundaries, this study presents a series of idealized simulations that attempt to replicate shear zones typical of drylines and other near-surface boundaries. The series of dry, constant potential temperature simulations are initialized with a north–south-oriented constant-vorticity shear zone and north–south periodic boundary conditions.

In all simulations, the shear zones develop wavelike perturbations that eventually roll up into discrete vortices. These vortices have features resembling those observed in many laboratory and numerical studies (i.e., instabilities developed into elliptical cores connected by vorticity braids that precess and contain pressure minima in their centers). To assess the instability mechanism, the results are compared to linear theory. Excellent agreement is found between predictions from linear theory for the wavenumber of maximum growth as a function of shear zone width and growth rate as a function of shear zone vorticity, suggesting to a very good first approximation, horizontal shearing instability (HSI) is responsible for the growth of initial small perturbations. It is also found that predictions of linear theory tend to extend well into the nonlinear regime.

Finally, preferred regions of cumulus formation are assessed by including moisture in four simulations. Maximum updrafts and simulated cumuli tend to form along the periphery of cores and/or along the braided regions adjacent to the cores. Because of the important modulating effect of misocyclone development via HSI and subsequent moisture transport, cumulus spacing and size/depth are also dependent on the shear zone width and vorticity.

1. Introduction

Coherent vortices are commonly observed features of fluid flows. In the atmosphere, vortices have been observed across wide-ranging scales. High-resolution observations of the planetary boundary layer (BL) have revealed the presence of small-scale misocyclones [i.e., vortices ~(1–4) km in width] along various surface-based boundaries (Crook et al. 1991; Atkins et al. 1995; Pietrycha and Rasmussen 2004; Kawashima and Fujiyoshi 2005; Arnott et al. 2006; Murphey et al. 2006; Marquis et al. 2007; Buban et al. 2007). Although there have been a plethora of observations of atmospheric vortices, the mechanisms by which vortices form and are maintained within a fluid initially void of vortices are not well understood on the smaller scales.

Various laboratory experiments have been conducted to study the instability of parallel shear flows. Winant and Browand (1974) found that unstable waves grow and the fluid is observed to roll up into discrete vortices after two streams of fluid of different velocities are brought together. Scotti and Corcos (1972) carried out an experiment on a statically stable free shear layer, where two uniform streams of air were brought together in a wind tunnel. They found unstable modes developing for Richardson number less than 0.25, as predicted theoretically by Miles (1961). Scotti and Corcos (1972) also calculated growth rates for various wavenumbers and Richardson numbers, and their results compared

Corresponding author address: Dr. Michael S. Buban, Atmospheric Turbulence and Diffusion Division, NOAA/OAR/Air Resources Laboratory, 456 S. Illinois Ave., Oak Ridge, TN 37830. E-mail: michael.buban@noaa.gov

DOI: 10.1175/JAS-D-14-0355.1

favorably with the numerical results for both the hyperbolic tangent and error function velocity profiles obtained by Hazel (1972).

Drazin and Howard (1962) derived general stability criteria for inviscid unbounded parallel flow. Their method, for fixed phase speed (c), was to seek asymptotic solutions to Rayleigh's equation by expansion into a power series in wavenumber (α). The dispersion relations for the piecewise-linear shear and rectangular jet profiles were calculated, with results consistent with linear theory. Hazel (1972) numerically computed stability characteristics for both the tanh and error function velocity profiles for various Richardson numbers. In the homogeneous case (Ri = 0), their results compare well with the experimental results of Scotti and Corcos (1972).

The numerical calculations for various free shear layers (e.g., Lessen 1950; Esch 1957; Betchov and Szewczyk 1963) have shown that the neutral stability curve asymptotically approaches the values determined from inviscid linear theory at large Reynolds numbers. Experiments have also shown that for large Reynolds numbers, the behavior of free shear layers is not appreciably affected by viscosity (e.g., Sato 1960; Schade and Michalke 1962; Michalke 1965; Balsa 1987).

Studies have also been conducted to numerically approximate the stability characteristics of parallel free shear flows. A constant-vorticity layer can be approximated by a vortex sheet in the limiting case of small wavenumbers (i.e., large wavelengths). The Kelvin–Helmholtz instability of an infinite vortex sheet has been numerically treated by Rosenhead (1931) with the inclusion of a nonlinear component. It is found that the initial instability grows exponentially, eventually leading to a rollup of the vortex sheet into discrete vortices. Pozrikidis and Higdon (1985) considered finite vortex layers consisting of constant vorticity to study the growth of periodic disturbances using a contour dynamics (CD) method. Their results show that the growth rates are a function of the shear layer width (that in turn is defined as a constant times wavenumber) and compare well with predictions based on linear theory. Guha et al. (2013) applied the CD technique and a quasi-inviscid direct numerical simulation (DNS) to a piecewise-linear shear layer and found that both the CD and DNS procedures agreed with linear theory. In the Pozrikidis and Higdon (1985) study, the initial wavenumber and shear zone width were fixed, with subsequent evolution examined. In the Guha et al. (2013) study, the domain size (initial wavenumber) and shear zone width were fixed at the predicted maximum growth rate from linear theory. Therefore, these studies could not determine whether given a large enough domain and arbitrary shear zone width, if the wavenumber of maximum growth rate predicted by linear theory would in fact emerge having not been forced by the initial conditions. Additionally, these studies were only 2D, so the effect of three dimensionality on real flows remained unanswered.

The environment in which vortices initiate, grow, and decay will modulate or even dictate the mechanisms by which these processes occur. The basic flow in which vortices eventually develop may contain differing amounts of preexisting vorticity that is modulated by shear zones possessing differing widths or magnitudes of shear. The present study is primarily focused on identifying the hypothesized horizontal shearing instability mechanism (HSI) from which small-scale vortices form, with applications to small-scale atmospheric vortices and their effect on sensible weather. Specifically, the present study is focused on vortices that form along a surface-based interface (i.e., boundary) that separates fluids with two different velocities. This interface takes the form of a finite-width shear layer with constant vorticity. In this study, a series of idealized simulations are conducted to test the HSI hypothesis. The simulations are set up with large enough domains so that a wide range of wavenumbers, including that of the maximum growth rate predicted by linear theory, would be allowed to emerge naturally. In addition to the horizontal shear zones, the initial environments are vertically homogeneous so the effects of three dimensionality on HSI can be tested. The present idealized simulations complement and extend a previous study of misovortex formation using observed initial and boundary conditions (Buban et al. 2012, hereafter B12).

Several studies have hypothesized that misocyclones may assist cumulus formation and convection initiation (CI) by rearranging the moisture and convergence fields (Pietrycha and Rasmussen 2004; Buban et al. 2007; Lee et al. 2000; Kanak 2008; B12). Therefore, identifying the mechanisms by which misocyclones form and their characteristic structure may further advance understanding of the process by which CI occurs along near-surface boundaries.

2. Model description

The simulations in the present study are conducted using the Collaborative Model for Multiscale Atmospheric Simulation (COMMAS) (Wicker and Wilhelmson 1995; Coniglio et al. 2006; Mansell et al. 2010; B12). COMMAS is a cloud-resolving and nonhydrostatic model, and it includes (weakly diffusive) fifth-order advection (Wicker and Skamarock 2002). All explicit mixing terms have been deactivated in the simulations. The lower boundary has been treated as free slip and the upper boundary as rigid. Since only shallow cumulus clouds are to be simulated, a simple Kessler warm-rain scheme was used to model the cloud microphysics.

For the idealized simulations, the base-state flow and the shear zone are assumed to be meridionally oriented and centered within the model domain. The simulations are run with periodic north–south boundary conditions and thus yield an essentially infinite-length channel. The simulation domain is configured with a 100-m grid spacing in both the horizontal and vertical directions. The domain size is 29.9 km in the meridional (along stream) direction, 14.9 km in the zonal (cross stream) direction, and 4 km in the vertical (i.e., $300 \times 150 \times 41$ grid points). The zonal domain size was chosen to be wide enough to mitigate the effects of boundary conditions and the meridional size was chosen to capture a wide range of wavenumbers. The vertical size was chosen to resolve the typical BL depth while being deep enough to minimize the influence of the upper boundary condition. As inferred from simulation results to be presented, the chosen grid spacing is hypothesized to adequately resolve commonly observed features along drylines (e.g., shear zone width, vertical vorticity bands and isolated vortices, updrafts) as well as the physical instability mechanisms leading to misovortexgenesis. Additional tests were run down to a 25-m grid, and although more finescale structure in the vortices was seen, on the scales for which this study is focusing, there was little difference. That is, the growth rates and wavelengths of maximum amplitude were the same.

The initial conditions for the simulations are produced by parametrically prescribing model variable fields. Most idealized simulations will be referred to as barotropic since they are dry (i.e., no water vapor or cloud processes) and contain a constant potential temperature within the entire domain. The initial u and w components of the wind are assumed to be zero everywhere. The v component is prescribed with a constant value on the west side of the domain, a constant shear zone in the center of the domain with a linearly increasing v component, and a constant value on the east side of the domain. This initial condition for the v component corresponds to the piecewise-linear shear zone employed by Rayleigh (1880). The piecewise-linear shear zone configuration consists of zero vorticity outside the shear zone, a constant vorticity inside the shear zone, and a vorticity discontinuity on each lateral boundary of the shear zone (Fig. 1).

The v component of the wind is also assumed to be constant with height. Therefore, the shear is purely due to the variation of the north–south wind component, and the initial vector vorticity everywhere is purely vertically oriented. To test the barotropic instability mechanism, a series of simulations are conducted by varying the width of the shear zone and the magnitude of the shear across the shear zone—thus varying the magnitude of the initial vorticity within the shear zone (Table 1). The range of shear zone widths and shear magnitudes were chosen to replicate the range of values typically found along real near-surface boundaries. As an example, observations from several mobile mesonet transects across a dryline on 22 May 2002 are shown (Fig. 2). In addition, a random v-component perturbation of 0.01 m s^{-1} is added to the initial wind field. Sensitivity tests that vary the x dimension of the model domain or impose a sinusoidal initial perturbation with random amplitude and phase in the y direction (Buban 2014, hereafter B14) essentially reproduce the results of the present study.

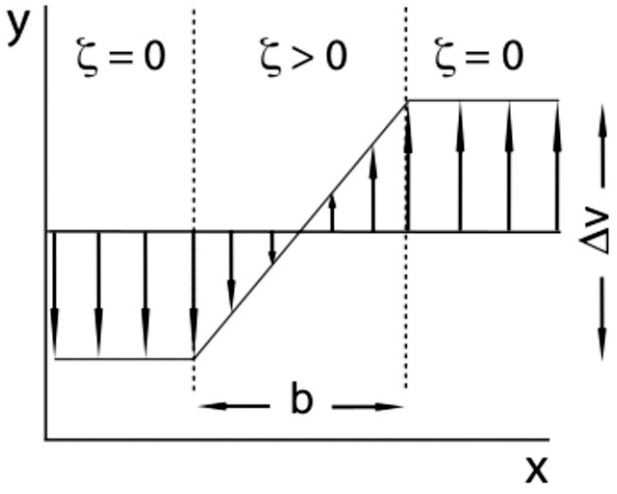

FIG. 1. Schematic setup of the idealized simulations. The environmental wind is shown at the center of the domain and is the same for all values of y. All symbols are defined in the text.

Cumuli and subsequent convection initiation often develop along discrete locations along near-surface boundaries [see Fig. 2 in Wakimoto and Murphey (2009) for the 22 May 2002 case]. Therefore, four additional "moist-barotropic" simulations are performed with moisture added while maintaining horizontal homogeneity in virtual potential temperature to assess preferred locations of cumulus formation. In these moist cases, the water vapor mixing ratio varied linearly from 6 to 9 g kg^{-1} from west to east across the shear zone at the surface and decreased everywhere 1.5 g kg^{-1} km^{-1} from the surface to the top of the domain. In addition, small static stability (a virtual potential temperature increase of ~1.7 K km^{-1}) was added everywhere to prevent cumuli from reaching their LFCs in the relatively shallow domain. Soundings to the east and west of the shear zone are shown in Fig. 3.

3. Analysis tools

a. *Linear theory*

The classic approach to studying instability of parallel free shear flows is to perform a linear stability analysis.

TABLE 1. Magnitude of the constant vertical vorticity ζ_0 ($\times 10^{-3}$) within the shear zone for each simulation.

Shear zone width	6 m s^{-1}	8 m s^{-1}	12 m s^{-1}	16 m s^{-1}	20 m s^{-1}	24 m s^{-1}
400 m	15	20	30	40	50	60
500 m	12	16	24	32	40	48
600 m	—	13.3	20	26.7	33.3	40
800 m	—	—	15	20	25	30
1000 m	—	—	12	16	20	24

If small perturbations are found to grow with time, the flow is unstable. The linear stability analysis procedure is briefly outlined as follows.

Assume that the flow is inviscid and incompressible and make the Boussinesq approximation, so the equations of motion take the form

$$\frac{\partial \mathbf{u}}{\partial t} + \mathbf{u} \cdot \nabla \mathbf{u} = -\frac{1}{\rho_0} \nabla p - \frac{\rho}{\rho_0} g \mathbf{k}, \tag{1}$$

where $\mathbf{u}$ is the velocity, p is the pressure, ρ is the density, g is the gravitational acceleration, ρ_0 is a constant reference density, and $\mathbf{k}$ is the unit vector in the vertical (z) direction. The continuity equation is written as

$$\nabla \cdot \mathbf{u} = 0 \tag{2}$$

and the thermal energy equation is expressed as

$$\frac{\partial \rho}{\partial t} + \mathbf{u} \cdot \nabla \rho = 0. \tag{3}$$

As described in section 2, the numerical model employed in the present study is based on a governing equation set with the same dominant physical processes (i.e., nonhydrostatic momentum and fluid temperature-density conservation) as assumed in Eqs. (1)–(3).

Next, we neglect any density variations and consider only the 2D problem (i.e., neglect the vertical dimension for HSI). The governing equations are then expanded by assuming that a given variable is the sum of the steady base state and a small perturbation. For example, u is expanded as $u(x, y, t) = U(x) + u'(x, y, t)$, where base-state

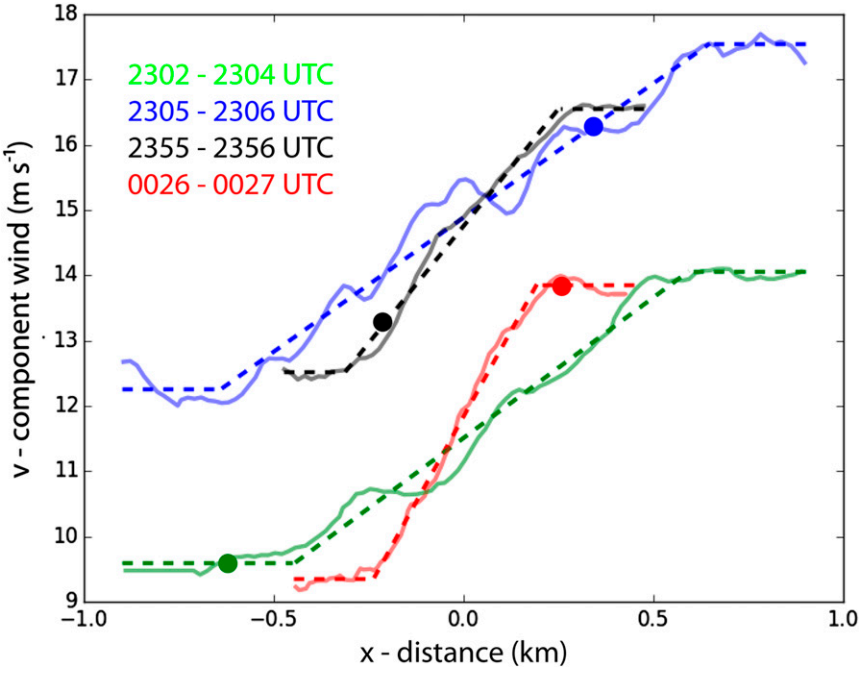

FIG. 2. Four mobile mesonet (MM) transects of a dryline on 22 May 2002 during the IHOP field project. The 1-Hz MM observations at slow highway transect speeds generate observations at about 20-m spatial resolution. Each color denotes a different transect and shows the variation of the v-component wind across the nearly north–south-oriented dryline. The x distance is measured from the center of the dryline. The colored dots indicate the approximate centers of the moisture gradient.

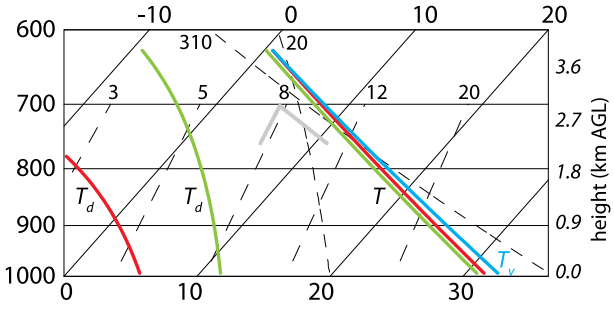

FIG. 3. Skew-T diagram of temperature (T), virtual temperature (T_v), and dewpoint temperature (T_d) to the east (green) and west (red) of the shear zone in the moist cases. The blue curve denotes the virtual potential temperature profile over the entire domain in all cases. The gray curves depict the conserved profiles of a 100-mb-layer-average lifted parcel with a cloud base at 700 mb and ~3 km AGL.

values are capitalized and perturbation quantities are primed. Substituting expanded variables into Eqs. (1)–(3) and neglecting terms involving products of perturbation quantities, there follows

$$\frac{\partial \mathbf{u}'}{\partial t} + V\frac{\partial \mathbf{u}'}{\partial y} + \frac{dV}{dx}u'\mathbf{j} = -\frac{1}{\rho_0}\nabla p' \quad \text{and} \tag{4}$$

$$\nabla \cdot \mathbf{u}' = 0, \tag{5}$$

which express the linearized inviscid equations of motion and mass continuity.

Then we seek normal-mode solutions of the form $v'(x, y, t) = \hat{v}(x)e^{ik(y-ct)}$ and introduce a streamfunction such that $u' = \partial\psi/\partial y$, and $v' = -\partial\psi/\partial x$. Defining the streamfunction as $\psi(x, y, t) = \phi(x)^{ik(y-ct)}$ leads to $\hat{u} = ik\phi$ and $\hat{v} = \phi'$ and finally,

$$(V - c)(\phi'' - k^2\phi) - V''\phi = 0, \tag{6}$$

where Eq. (6) is termed the "Rayleigh stability" equation.

The Rayleigh stability equation describes an eigenproblem for the eigenvalue c and the eigenfunction ϕ in terms of the arbitrary profile of V. Equation (6) together with the boundary conditions

$$k\phi = 0 \quad \text{at} \quad x = \pm\infty \tag{7}$$

(which ensure that u' goes to zero at $\pm\infty$ and where here k is the critical wave number) define the basic eigenvalue problem for free shear layers.

For the piecewise-linear shear layer, the resulting solutions are exponential functions within each subregion—for example,

$$\phi(x) = \begin{cases} Ae^{-k(x-b)} & (x > b) \\ Be^{-k(x-b)} + Ce^{kx} & (0 < x < b) \\ De^{kx} & (x < 0) \end{cases}. \tag{8}$$

Using Eq. (8) in (6) and applying matching conditions to ensure continuity of pressure and normal velocity at each interface [see Heifetz et al. (1999)] results in an expression for the complex phase speed

$$c^2 = \frac{V_m^2}{b^2}[(kb - 1)^2 - e^{-2kb}]. \tag{9}$$

Here $-V_m$ is the base-state velocity west of the shear zone and V_m is the velocity east of the shear zone. The condition $c^2 > 0$ in Eq. (9) represents two neutrally stable waves that travel in opposite directions. Conversely, the condition $c^2 < 0$ represents two stationary waves, where one wave is unstable and the other wave is stable. Setting $[(kb - 1)^2 - e^{-2kb}] = 0$, we find that the shear layer with critical wavenumber $k = 1.28/b$ is only unstable for wavenumbers $0 < k < 1.28/b$ and stable otherwise. The most-unstable wavenumber is $k \approx 0.8/b$. A plot of Eq. (9) is shown in Fig. 4.

b. Spectral density estimation

To compare the idealized simulations to the results of linear theory, spectral density estimation is performed on spatial series within the shear zone in the meridional or downstream direction (B14). For example, it is imperative to quantitatively compare the theoretical most-unstable wavenumber against the fastest-growing wavenumber in the various simulations. The spectral density estimation follows the smoothed autospectral procedures described by Jenkins and Watts (1969, hereafter JW69).

The evolving spatial series of variables [e.g., u, v, and ζ (vorticity)] are output in the downstream direction within the shear zone of each simulation. The mean values of each variable are computed and subtracted from each detrended series, the autocovariance functions are computed, and a lag (Tukey) window is applied to calculate the resulting smoothed spectral estimates. By choosing the truncation point (M), the lag window controls the degree of smoothness of the resulting spectral analysis. The truncation point defines the number of terms used in the spectral estimate calculation for each wavenumber. Smaller values of M produce smoother estimates (but may introduce larger biases in the spectral peak), while larger values of M retain more variance in the spectral estimate with smaller bias of the spectral peak (JW69). To test the spectral estimation procedure, a known function was also used to generate artificial spatial series of data. These data were then run through the spectral estimate procedure with varying truncation points. The truncation point of $M = 100$ gave the best results in terms

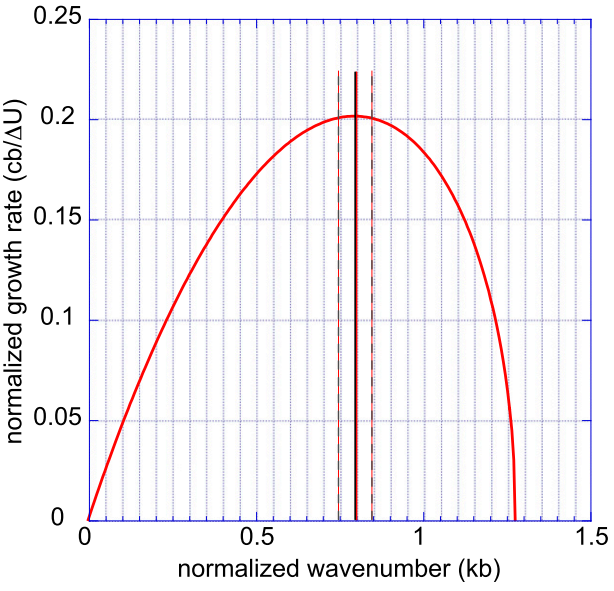

FIG. 4. Normalized growth rate as a function of wavenumber as defined by Eq. (9). The (nearly coincident) vertical solid red and black lines (i.e., the theoretical and mean simulated most-unstable normalized wavenumbers, respectively) and the vertical gray dashed lines to the left and right of the red–black lines are referenced in Fig. 9.

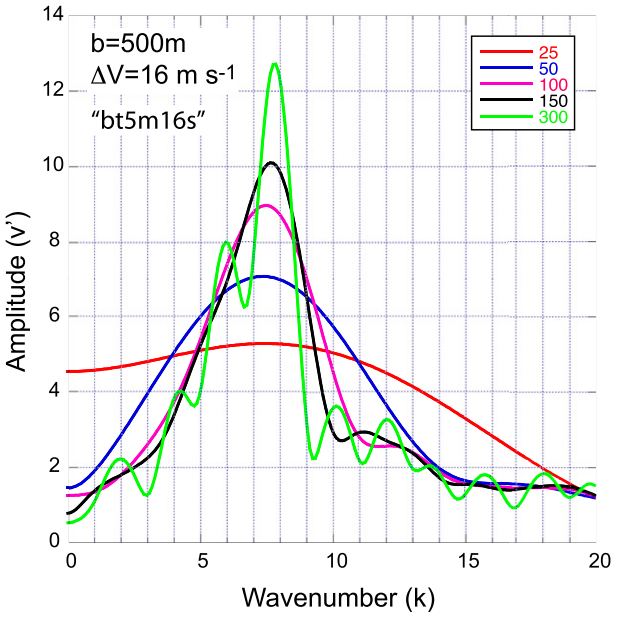

FIG. 5. Spectral density estimates at five different truncation points—25 (red), 50 (blue), 100 (magenta), 150 (black), and 300 (green)—for the idealized simulation case with a shear zone width of 500 m and a shear magnitude of 16 m s^{-1}. This simulation will be called bt5m16s in future references. The value of the truncation point used in this study (M = 100) corresponds to the magenta colored curve. The amplitude (square root of the variance) is plotted in all spectral estimates.

of bias and smoothing and yielded similarly good results with simulation data spatial series via minimized bias and maximized smoothing to eliminate spurious sidelobe peaks (Fig. 5).

Finally, spectral estimates were averaged over wavenumber space. This variance is distributed over a continuous range of wavenumbers, so that on a plot of spectral density estimates (e.g., Fig. 5), the area under the curve is equal to the percentage of the variance of the series explained by the wavenumbers in the range from k to $k + \Delta k$.

4. Results

All simulations have a similar evolution, which for conciseness may be summarized as follows. From the initial state, characterized by a region of constant vorticity bordered on the east and west by regions of zero vorticity, the simulations progress by maintaining a nearly homogeneous, constant-vorticity, constant width vorticity layer for a considerable time. Following initialization, there is a brief spinup period (roughly ~200 s) wherein small perturbations are damped, followed by exponential growth of preferred wavenumbers consistent with predictions of linear theory. Eventually, as the initial perturbations have grown by about two orders of magnitude, wavelike features emerge along the shear zone. These wavelike features continue to amplify and eventually develop into discrete vortices.

a. *Evolution of shear zones*

One simulation (bt5m16s) is shown in detail to generally represent typical behavior manifested in all simulations. Here the nomenclature is bt for barotropic, 5m for 500-m shear width, and 16s for 16 m s^{-1} shear. The shear zone is characterized by the emergence of small-amplitude waves by ~1500 s (Fig. 6). These waves continue to grow in amplitude exponentially as quantified by spectral analysis (shown later) and eventually roll up into discrete vortices between 1560 and ~1800 s (Figs. 6b–f). This process can be better visualized in the vertical vorticity fields with wavelike perturbations in the shear zone and isolated pockets of enhanced vorticity developing by ~1500 s (Fig. 7a). These wavelike perturbations grow exponentially as vorticity is concentrated into discrete cores between 1560 and ~1800 s (Figs. 7b–f). The emerging structure is dominated by a peak around wavenumber 8.

b. *Perturbation wavelengths*

Linear theory predicts the most-unstable wavenumber (k) to be ~0.8/b or a most-unstable wavelength

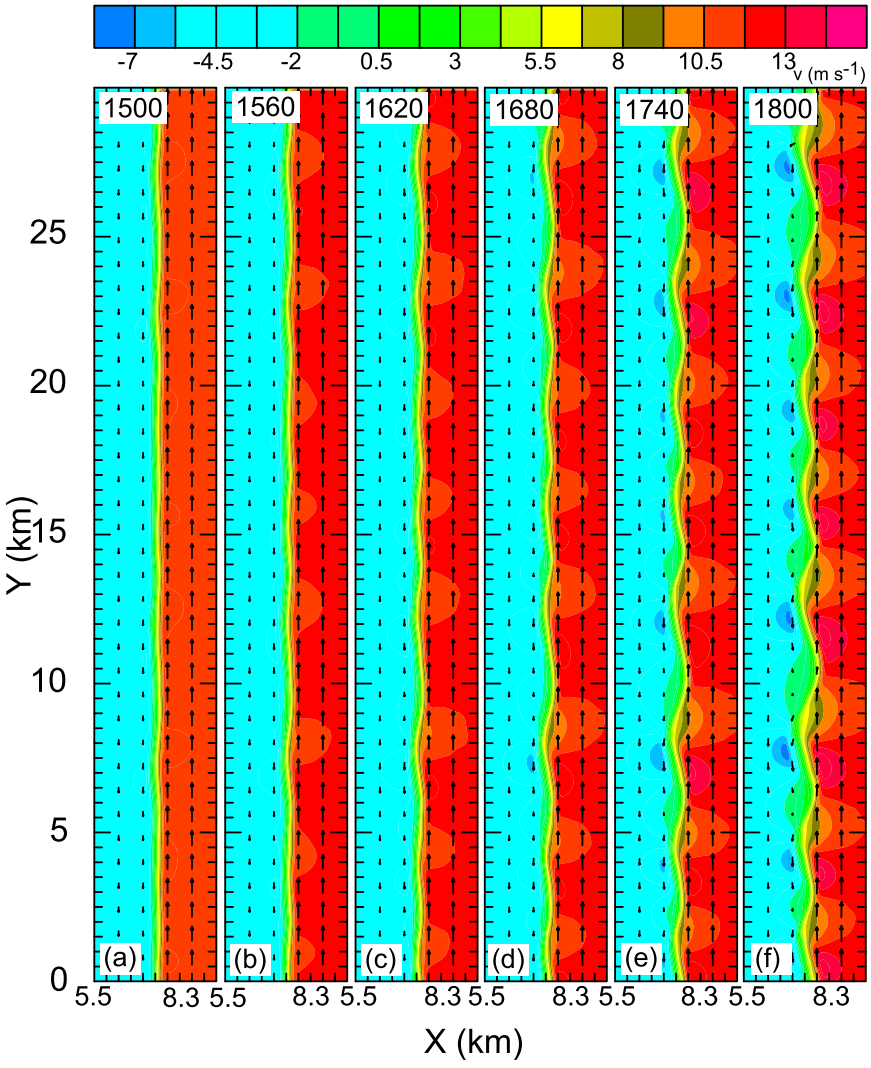

FIG. 6. (a)–(f) Meridional (v component) wind (colors) and horizontal wind vectors (500 m distance in y equivalent to 10 m s^{-1}) through the center of the simulation domain ($z = 2$ km) vs time from 1500 to 1800 s for the bt5m16s case.

($l = 2\pi/k$ of ~7.9b, where b is the width of the shear zone.[1] Therefore, with time, an arbitrary exponentially growing initial disturbance should become dominated by a wavelength close to that of the most-unstable mode, as long as the disturbance amplitudes are small enough for linear theory to be valid.

Spectral density estimates at successive times show the perturbation amplitude evolution as a function of wavenumber for the bt5m16s case (Fig. 8). It is seen that growth occurs at nearly all wavenumbers at all times. Initially, a weakly defined triple peak emerges by ~1050 s around wavenumbers 3 and 16, transitioning to a single strong peak at wavenumber 7.5 ($\lambda = 4000$ m) between 1320 and 1560 s. This wavenumber is very close to the theoretically predicted most-unstable wavenumber of 7.6 ($\lambda = 3950$ m).

Note that the spectra are only displayed to wavenumber 30 to depict the wavenumbers that are substantially growing. Growth rates are observed to monotonically decrease with increasing wavenumber in all cases (not shown) so that at large wavenumbers the spectra asymptotically approach the spectra of white noise with an amplitude equal to the magnitude of the initial perturbation. Thus the wavenumber 0–30 band isolates the significant growth across all cases.

[1] Note that in all subsequent references, we will be discussing a domain-relative wavenumber, $\kappa = kL/2\pi$, and wavelength, $\lambda = 2\pi/\kappa$, where $L = 29\,900$ m is the north–south domain length. For example, wavenumber 5 comprises five waves of length 5980 m that span the north–south domain.

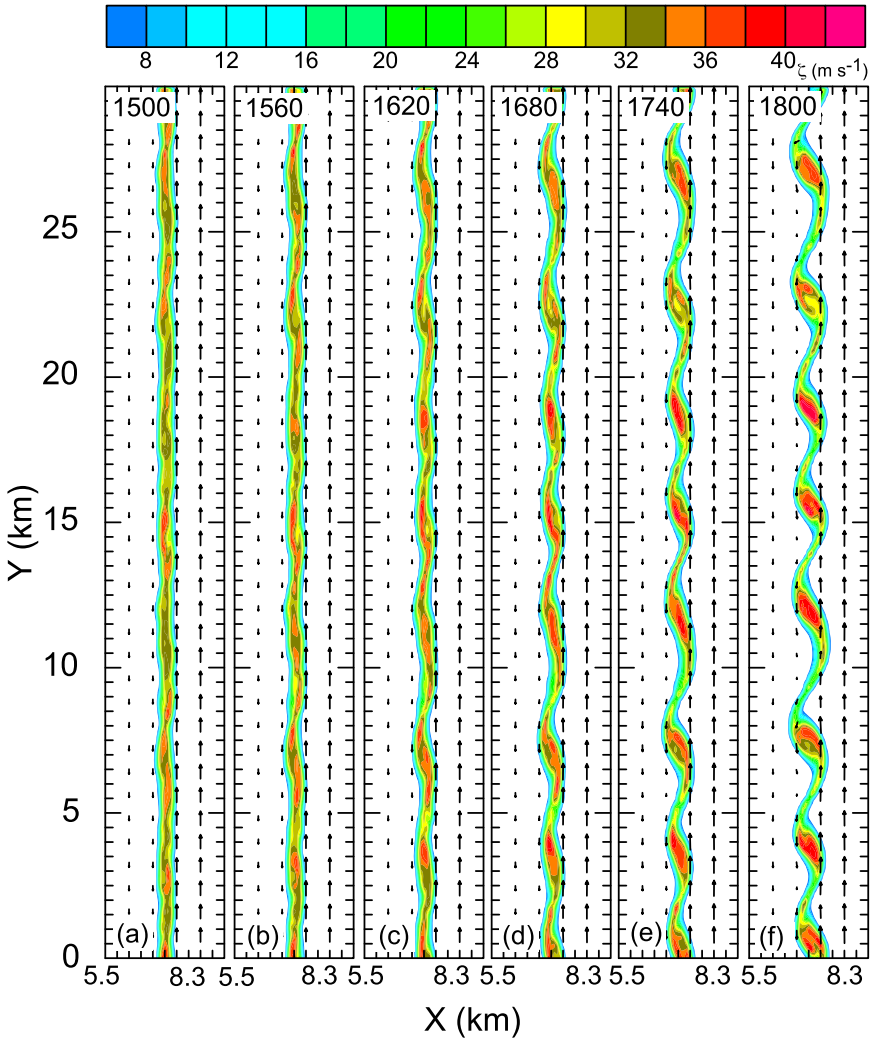

FIG. 7. As in Fig, 6, but for vertical vorticity ζ (colors) instead of meridional wind.

Transient initial growth is seen across all wavenumbers in all simulations. Later, some growth is seen even at wavenumbers larger than the theoretical neutral wavenumber where linear theory predicts stability. One limitation of linear theory is that it ignores any nonexponential (i.e., algebraic) growth, the latter state being possible in real fluids (Pedlosky 1987). Each normal mode is further assumed to grow independently, so any potential growth due to nonorthogonal interaction among the modes is ignored (Farrell 1984; Trefethen et al. 1993; Heifetz and Methven 2005). In all simulations, small-amplitude growth is occurring that cannot be explained by linear theory. Determining the nature of this growth is beyond the scope of this study. However, it is the exponential growth that can be explained by linear theory that with time dominates the spectrum, thus describing the emerging structure at later times.

The simulations all behave similarly across the range of shear zone widths and shear magnitudes in terms of the peak amplitude in the spectral density estimates at the later stages of exponential growth when perturbation amplitudes are relatively high and linear theory is still valid (Fig. 9a). The actual wavenumbers of maximum perturbation amplitude are close to the theoretical most-unstable wavenumbers. For a given shear zone width, the differences in wavenumber are small across the various shear magnitudes, ranging from 0.1 for the 800-m cases to 0.5 for the 400-m cases (although this corresponds to a wavelength of about 150 m in both). However, there is a small high bias in the 400- and 1000-m simulations and a small low bias in the 800-m runs compared to the theoretical values. By normalizing the wavenumbers according to shear zone width, the simulations can be compared to one another and to the theoretical most-unstable wavenumber (Fig. 9b).

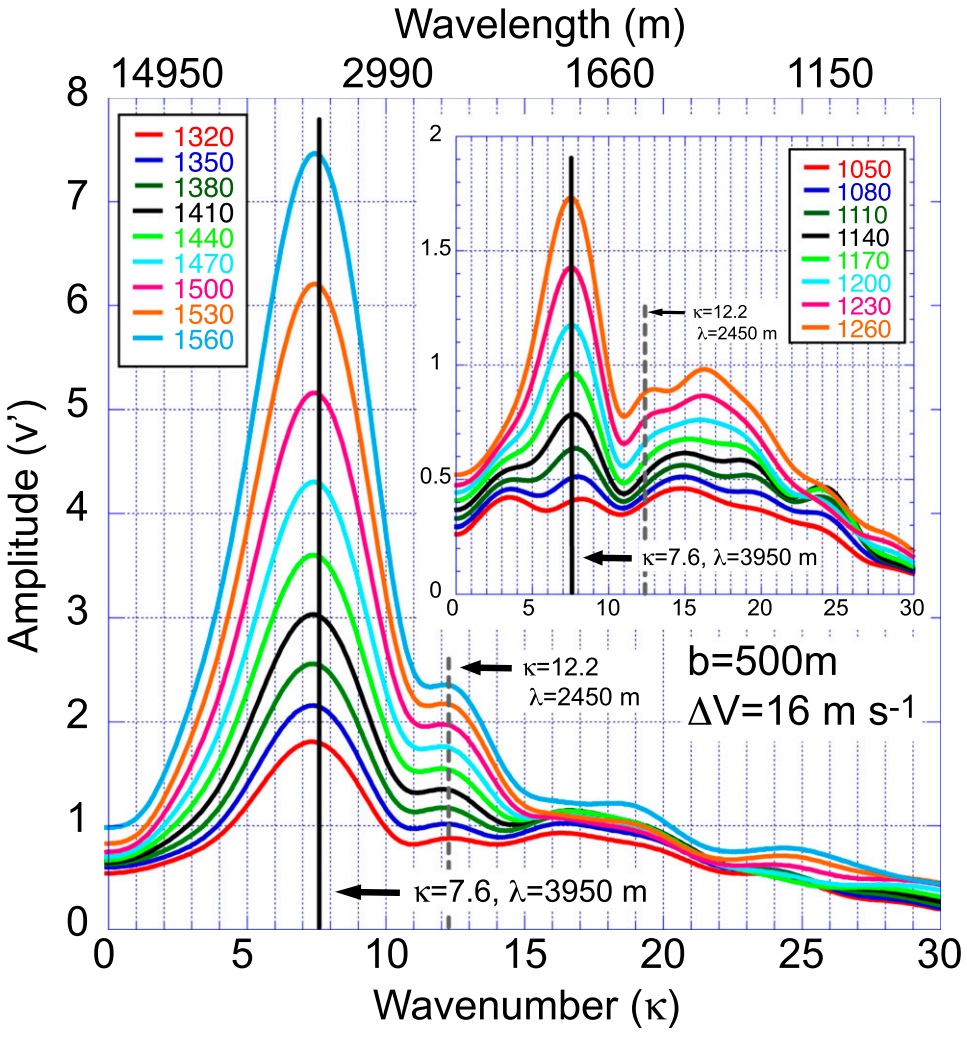

FIG. 8. Spectral density estimates of the v-component perturbation wind amplitude (m s^{-1}) as a function of wavenumber for the period of 1320–1560 and 1050–1260 s (inset) after the start of simulation bt5m16s. The vertical black line denotes the most-unstable wavenumber (7.6) and the dark gray dashed line denotes the neutral wavenumber predicted by linear theory (12.2).

Across the 25 simulations, the mean peak amplitude (0.7944) is extremely close to the theoretical most-unstable wavenumber (0.7969), with a small standard deviation (0.0532). It is seen that most of the variance is clustered near the theoretical peak in a region where the stability curve is relatively flat (Fig. 4). Thus, the maximum growth wavenumber is adequately being explained by linear theory. The dimensional simulated maximum-amplitude wavelengths as a function of shear zone width are also rather highly correlated with the theoretical value of 7.9b (Fig. 10).

c. *Perturbation growth rates*

The growth rates are computed from the change in the spectral estimates with time. For all the cases, there is a strong linear relationship between the magnitude of the shear and the growth rates, with larger growth rates corresponding to larger shear values (Fig. 11). The linear correlation between the growth rate and shear magnitude is high for the 800-m shear zone widths ($R \sim 0.98$), even higher for the 600- and 500-m widths ($R > 0.99$), and is essentially exact for the 400-m case ($R = 1.0$) to the degree of precision of the calculations (i.e., to five decimal places).

The computed growth rates from the simulations are smaller than the growth rates predicted by linear theory; however, this bias tends to decrease at smaller shear zone widths. In terms of the functional relationship between shear magnitude and growth rate for a given shear zone width, the theoretical and simulated results are in excellent agreement (Fig. 11). Linear theory predicts that the maximum growth rate varies

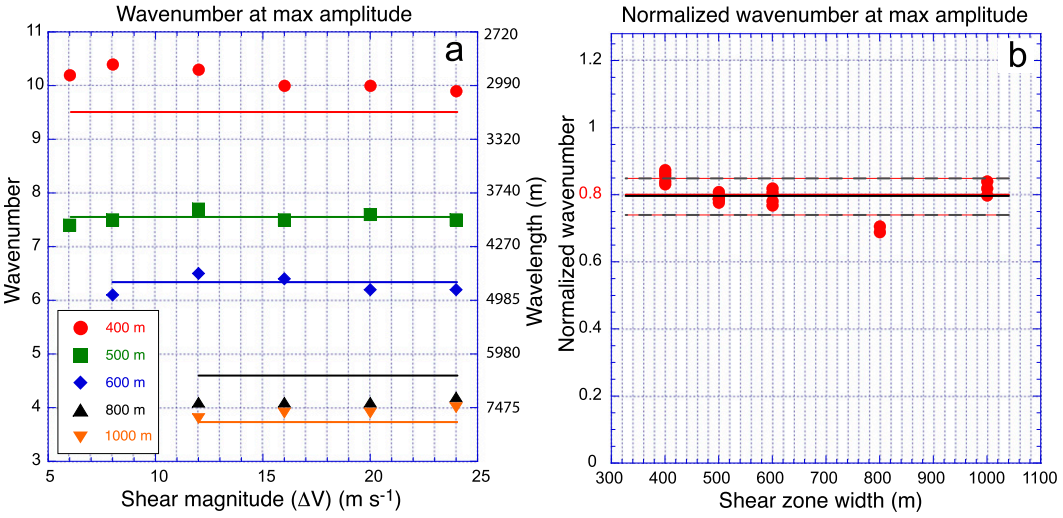

FIG. 9. (a) Wavenumber (wavelength) of maximum amplitude of the perturbation spectral density estimate for all simulations (markers) during the later phase of exponential growth (i.e., peak in curve at latest time in Fig. 8) vs shear magnitude (ΔV). The horizontal lines indicate the theoretical most-unstable wavelength for a given shear zone width (color). (b) Normalized wavenumber of maximum amplitude (markers), where the data were normalized by the shear zone width and domain length via the relation $\kappa = 2\pi k/L$, as a function of shear zone width. The horizontal red line nearly coincident with the black line is the theoretical most-unstable normalized wavenumber (0.797). The horizontal black line is the mean normalized wavenumber (0.794) and the horizontal dark gray dashed lines are plus or minus one standard deviation (0.053) from the mean.

as a function of the shear zone vorticity. Combining the four panels in Fig. 9, the growth rates are plotted as a function of shear zone vorticity (Fig. 13). There is a strong linear dependence of growth rate on the shear zone vorticity across all simulations as a whole (R = 0.989). The actual functional relationship between shear zone vorticity and growth rates (i.e., the slope of the curves in Fig. 12) in the simulations agrees with linear theory to better than one percent (i.e., simulated slope of 0.1997 versus theoretical slope of 0.2012). Therefore, although the spatial structure of the evolving shear layer depends only on the shear zone width, the dynamics that govern the temporal growth depends only on the vorticity magnitude and not on the shear zone width or shear magnitude independently.

d. *Phase shift and initial length*

Wave interaction theory (WIT) predicts that the growth of instabilities occurs once the two vorticity waves propagating along the shear zone vorticity discontinuities become phase locked (i.e., Heifetz et al. 1999; Heifetz and Methven 2005; Carpenter et al. 2013; Guha et al. 2013). Phase locking occurs when the phase shift between the two waves promote exponential growth of each wave. The phase shift is predicted to be $\phi = \cos^{-1}[(1 - 2\alpha_n)e^{2\alpha_n}]$ from linear theory (Guha et al. 2013), where α_n is the normalized wavenumber of maximum growth. A series of phase shifts were calculated for each case by examining the vorticity fields (e.g., Fig. 5) during the emergence of well-defined vortices. A total of eight individual waves were examined in each case (Table 2). The most-unstable wavenumber predicted by linear theory corresponds to a theoretical phase shift of 0.35π rad. The phase shifts calculated from the simulations are close to the predicted values (ranging from 0.30π to 0.38π rad), indicating that the wavenumber that eventually emerges has a phase shift in accord with WIT.

Knowing the phase shift, we can calculate the initial length of what will eventually become the resulting vortex core as $l_{\text{init}} = [1 + (\phi/\pi)](\lambda/2)$, where l_{init} is the normalized wavelength (Guha et al. 2013), corresponding to the most-unstable mode. The computed values are consistent with the initial lengths corresponding to the most-unstable wavenumber predicted by linear theory (Table 3). However, the initial lengths had a low bias in all four simulations.

e. *Nonlinear evolution*

Although it is beyond the scope of this research to study the fully nonlinear dynamics of the resulting vortices, some aspects of the rollup of vortices may be described and compared to other observed and simulated vortices. As the shear zone continues to roll up into discrete vortices, the flow saturates (i.e., perturbations reach a maximum) around 1920 s into the simulation

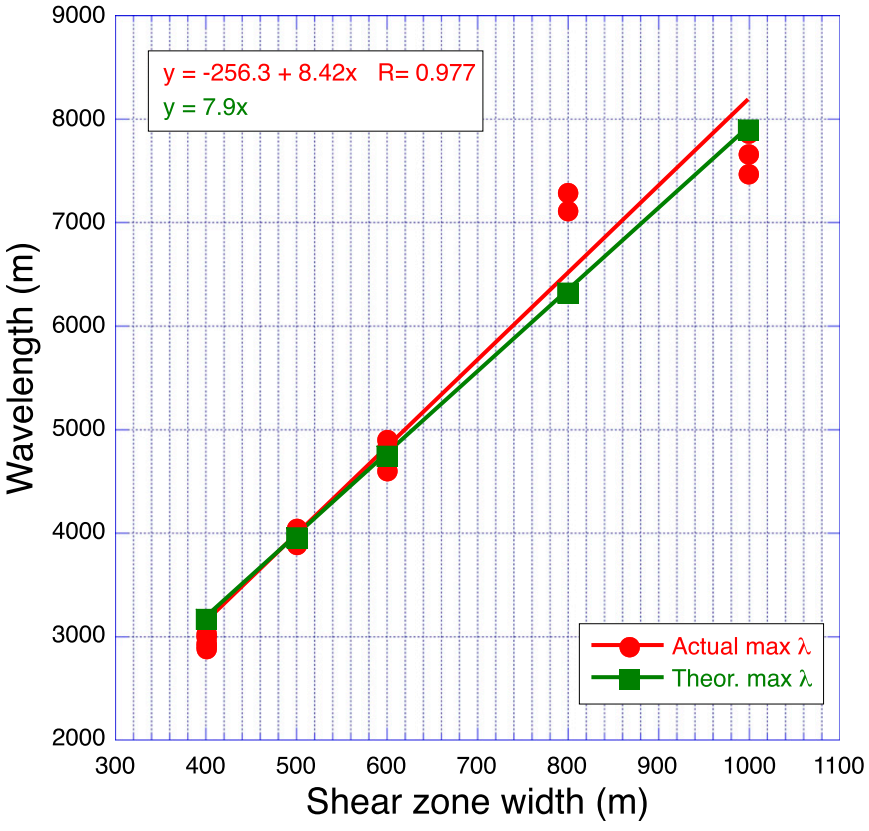

FIG. 10. Wavelength of maximum amplitude of the perturbation spectral density estimate for all barotropic simulations (red circles) during the later phase of exponential growth and the theoretical most-unstable wavelength (green squares). The best-fit lines are shown along with their equations.

(Fig. 13). At this time, there is a maximum perturbation in the positive (negative) v-component velocity on the east (west) sides of the circulation and a positive (negative) u-component velocity on the south (north) side corresponding to a velocity couplet and a vortex with positive vertical vorticity (Fig. 13). Nonlinear effects eventually dominate as the vortices continue to evolve in the period 1980–2160 s (Figs. 11c–f, Figs. 12c–f).

In terms of vorticity structure (Fig. 14), nearly equally spaced elliptical vortex cores develop that are separated by bands or braids of vorticity. With time, these braids become elongated and begin to completely wrap around the central vortex core. The elliptical vortex core itself rotates at constant angular velocity.

The core also nutates as the core aspect ratio (i.e., the ratio of the major and minor axis of the ellipse) undergoes a periodic oscillation. This was also seen in the simulation by Guha et al. (2013). Once the core reaches saturation, the vorticity within the core evolves in a somewhat complicated manner. In all vortices, there is a slight decrease with time of the magnitude of the central vorticity, although in some vortices this relative weakness is in the center whereas in others it is displaced to one side. As the vortices evolve, vertical motions develop with maximum amplitudes of about ~(2–3) m s^{-1}. Although the strongest vertical motions are near the vortex core, weaker vertical motions develop along the braids. Other observational studies have also found the strongest vertical motions near the vortex core (e.g., Wilson et al. 1992; Arnott et al. 2006; Marquis et al. 2007; B12; Campbell et al. 2014). The vertical motion field associated with the vortices displays some variability. The vertical motion field may consist of an upward–downward motion couplet with centers on either side of the vortex, or else with weak downward motion within the vortex and no exterior updraft, or else with an updraft surrounding the vortex and a downdraft in the center.

The pressure fields are characterized in all vortices by a pressure perturbation minimum in the center of each vortex and a local pressure perturbation maximum between each vortex in the braid regions (Fig. 15). The pressure perturbation field remains fairly constant outside the vortex cores, with both the local maximum and minimum elliptical regions featuring a nearly east–west-oriented major axis. Conversely, within the vortex cores

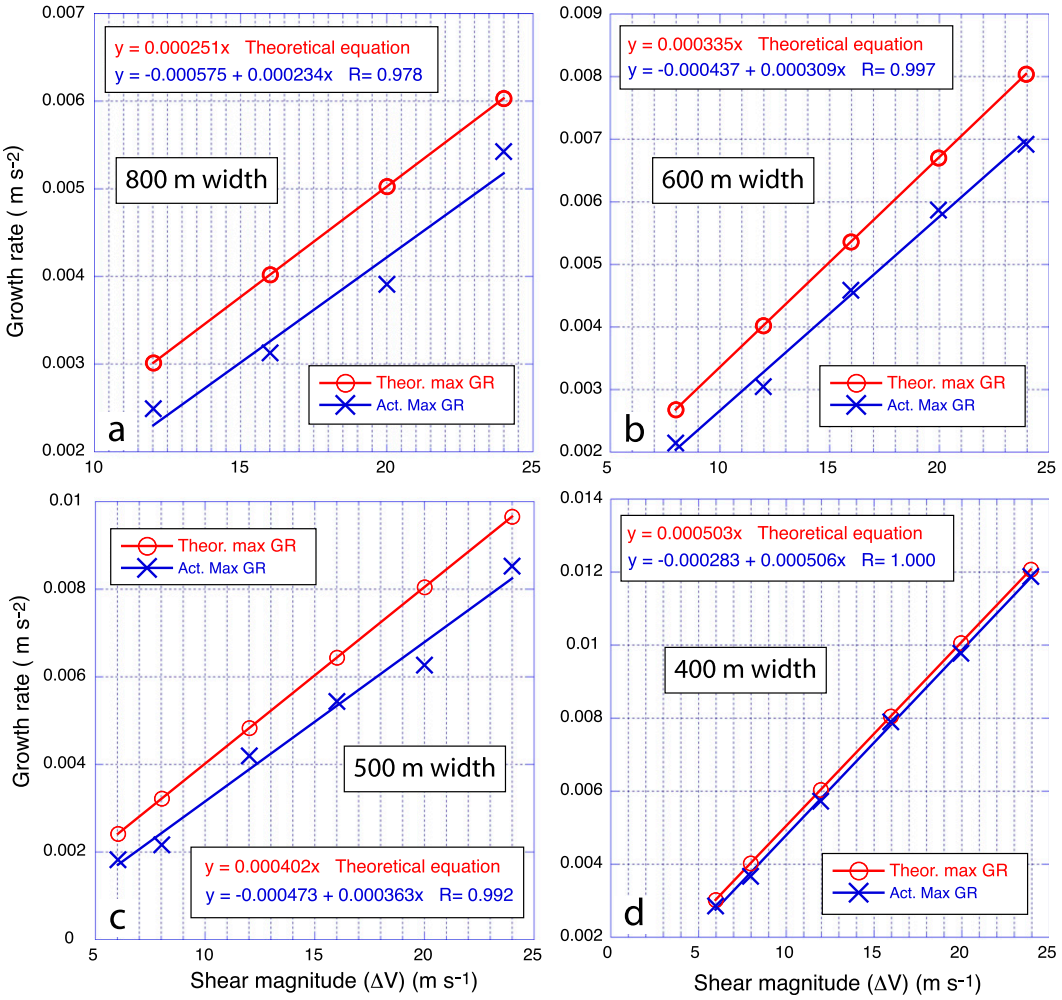

FIG. 11. Maximum growth rates (blue) plotted as a function of shear magnitude for four different shear zone widths (800, 600, 500, and 400 m). Also plotted in red are the theoretical maximum growth rates. Lines indicate linear least squares fits to the data points. Also shown are the least squares line equations and the correlation coefficients of these fitted lines.

the major axis of the pressure minimum rotates nearly at the angular velocity of the vortex itself.

In general, the size of the evolving vortices increases as the areal coverage and magnitude of the vorticity in the braids between the vortices decreases. It is also interesting to note that the vortex type is repeated every fourth vortex. That is, there is a wavenumber-2 component to the series of vortices (i.e., each vortex type is repeated twice in the simulation domain). Note that as the mature vortices near saturation the localized updraft maxima approach a nearly constant average value (Fig. 14). Although the detailed nonlinear stage of evolution has been shown for only one case, we can compute the average local maxima in vertical motion as each case reaches vortex saturation and compare the results (Fig. 16).

For a given shear zone width, the average local vertical motion maximum also increases as the magnitude of the shear increases. Across each shear zone width series, the correlation between the magnitude of the maximum vertical motion and the magnitude of the shear is very high [$R \sim (0.978–0.999)$]. There is a generally decreasing slope of the best-fit lines with increasing width. This decreasing slope is most pronounced between the 600- and the 800-m cases (Fig. 16). Note that the 1000-m cases (not shown) also have a slope that is smaller than the 800-m cases.

Since the growth rate and subsequent vortex strength is proportional to the shear zone vorticity, the maximum vertical motion and shear zone vorticity are also related (Fig. 17). The localized updraft maxima increase with the shear zone vorticity across all simulations with a fairly high degree of correlation ($R = 0.89$). This suggests that the magnitude of the subsequent local updraft maxima associated with mature vortices can be diagnosed given a

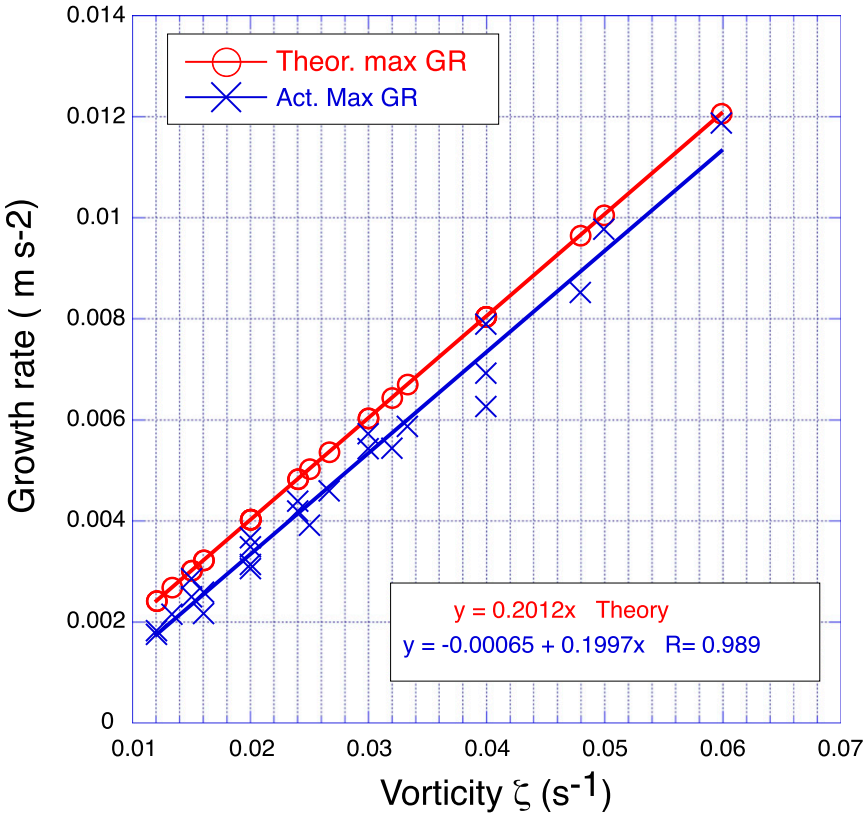

FIG. 12. Maximum growth rates (blue) plotted as a function of vorticity for all barotropic simulations. Also plotted in red are the theoretical maximum growth rates. Lines indicate linear least squares fits to the data points. Also shown are the least squares line equation and the correlation coefficient of these fitted lines.

known magnitude of the initial shear zone vorticity (or vice versa).

f. Cumulus formation

Although all simulations with moisture produce clouds in preferred regions, an example is shown for case mbt5m16s (where the additional "m" in the prefix indicates a moist simulation). The moisture fields associated with the evolving vortices display the classic Kelvin–Helmholtz (KH) billow wave pattern (although most previous KH billow examples involve waves in a vertical plane), with moist and dry air wrapping around the vortex center (Fig. 18). The modeled cumuli are associated with the stronger updrafts, with the deepest, strongest updrafts producing the largest and deepest cumuli. Note that although the peak in each local updraft is centered on the moisture gradient on the west

TABLE 2. Calculated phase shift (rad) from four simulations (including eight individual developing waves per simulation). Also shown are the averages for each case and the predictions of linear theory.

Waves	4m12s	5m16s	8m20s	10m24s
1	0.37π	0.36π	0.29π	0.34π
2	0.33π	0.40π	0.27π	0.38π
3	0.31π	0.32π	0.31π	0.41π
4	0.36π	0.39π	0.32π	0.39π
5	0.41π	0.39π	0.29π	0.40π
6	0.32π	0.30π	0.30π	0.39π
7	0.38π	0.38π	0.33π	0.34π
8	0.38π	0.37π	0.31π	0.36π
Average	0.36π	0.36π	0.30π	0.38π
Linear theory	0.35π	0.35π	0.35π	0.35π

TABLE 3. As in Table 2, but for initial length (m).

Waves	4m12s	5m16s	8m20s	10m24s
1	1840	2700	4640	4730
2	1730	2160	4000	5170
3	1620	2480	4110	4730
4	1730	2810	3890	4950
5	1730	2480	3890	5280
6	1620	2380	3890	4840
7	1890	2700	4750	4730
8	1890	2270	4000	4840
Average	1760	2500	4150	4910
Linear theory	2130	2660	4300	5320

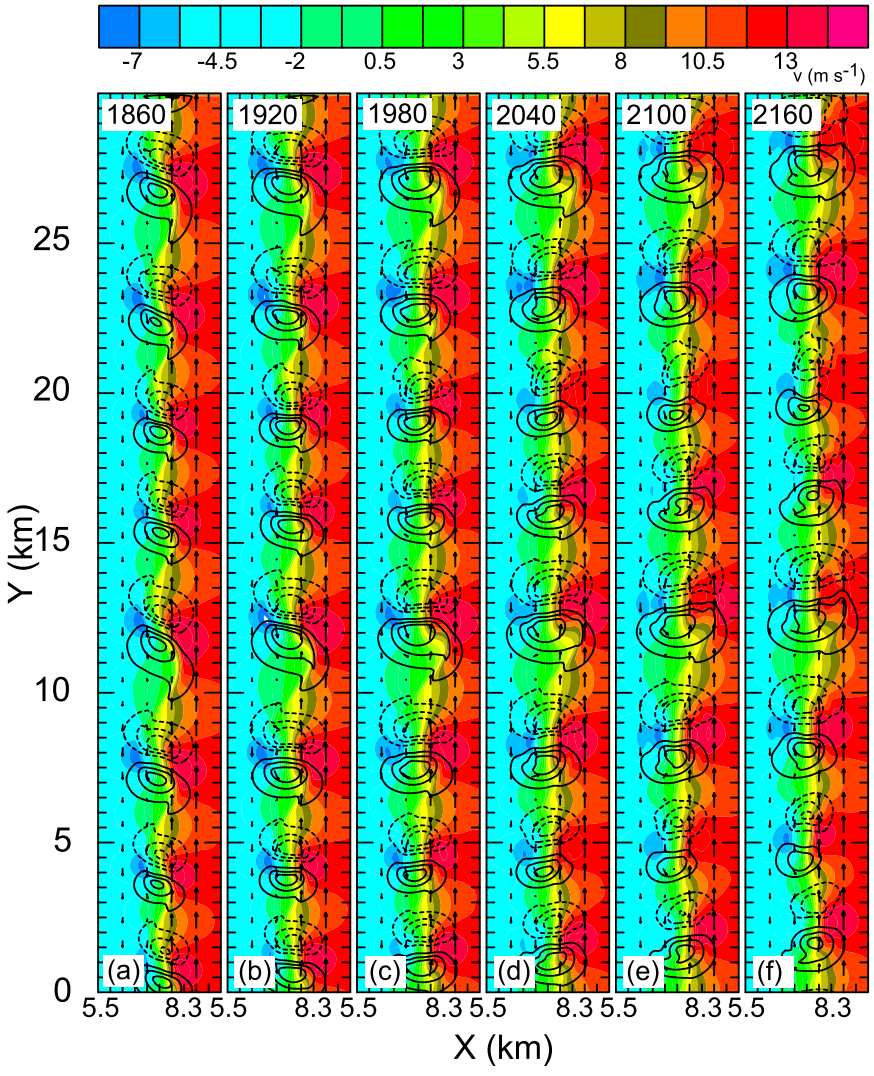

FIG. 13. As in Fig. 6, but for 1860–2160 s with solid (dashed) contours denoting westerly (easterly) flow at 1 m s^{-1} intervals starting at 1 (-1) m s^{-1}.

edge of the core, nevertheless the modeled cumuli form to the west of the maximum updraft. In other words, cumulus formation is forced within weaker (but still locally strong) updrafts that are juxtaposed with higher moisture values in the region between the vortex core and adjoining braid to the west.

Evolution of the vorticity and cloud water mixing ratio at 3 km are shown for the mbt5m16s case (Fig. 19). Clouds have formed by about 1980 s between the wrapping braid region and the core west of several mature vortices. Also, the developing cumuli grow larger with time. Note again the wavenumber-2 modulation of the vorticity fields and the resulting cloud pattern. Of the eight discrete vortices, two contain the largest developing cumuli of roughly the same size and shape, two contain smaller cumuli of roughly the same size and shape, and four do not develop cumuli. Note that the vertical motions in the mbt5m16s case are smaller than in the corresponding dry bt5m16s case owing to the inclusion of small static stability. Although only one moist simulation is shown, the locations of developing cumuli in relation to the vortex are identical in all moist simulations.

A conceptual model has been developed to elucidate the vertical motion and moisture structure leading to cumulus formation (Fig. 20). This conceptual model is developed based on the third vortex from the top in the bc5m16s case, which broadly typifies cumulus formation in the misocyclones (Figs. 18–19). Moist air originates at low levels northeast of the vortex core, adjacent to the northern vortex braid. The moist air enters the updraft to the northwest of the vortex core and is wrapped

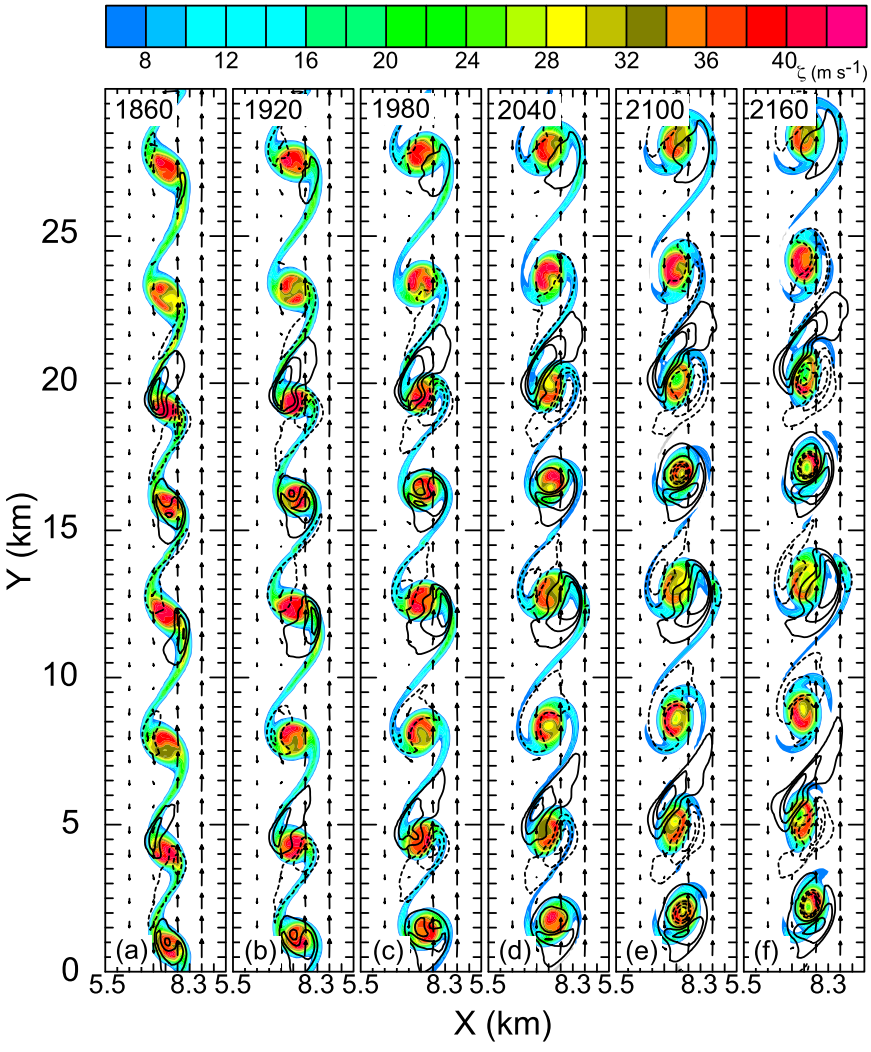

FIG. 14. As in Fig. 13, but for vertical vorticity with the solid (dashed) black contours denoting positive (negative) vertical velocity at 1 m s^{-1} intervals starting at 1 (-1) m s^{-1}.

around counterclockwise while ascending to cloud base. To the southwest of the vortex core, dry air from the mid- and upper levels wraps counterclockwise and descends to the southeast of the vortex core. In the center of the vortex core, both moist and dry air mix within a weak updraft or the axial downdraft. Note that in all vortices, the strongest upward motions are removed from the vortex core and are located either within or adjacent to the vorticity braids where there is strong deformation of the flow. The injection of moisture along the northern trajectory preferentially forces cloud formation along the northwestern braid. Similar vertical motions have been previously described by the process known as the "liftup effect," whereby the differential crosswise perturbation velocities tilt the background vertical vorticity (Vitoshkin et al. 2012).

5. Discussion

a. Comparison with linear theory

Linear theory is only applicable when the magnitude of the perturbations is "small." Although there is no well-defined cutoff for the transition from the linear to the nonlinear regime, one metric to assess the degree of linearity (i.e., the extent to which products of perturbations can be neglected compared to some measure of the mean flow) is to compare the amplitude of the perturbation in the v-component wind to the v-component shear across the shear zone (i.e., peaks in the curves in Fig. 6). If a' is the amplitude of the maximum v' perturbation, then the ratio $L = 2a'/\Delta V$ is a measure of the percentage of the mean flow contained in the perturbation. Across the simulations, it appears that the growth described by linear theory holds

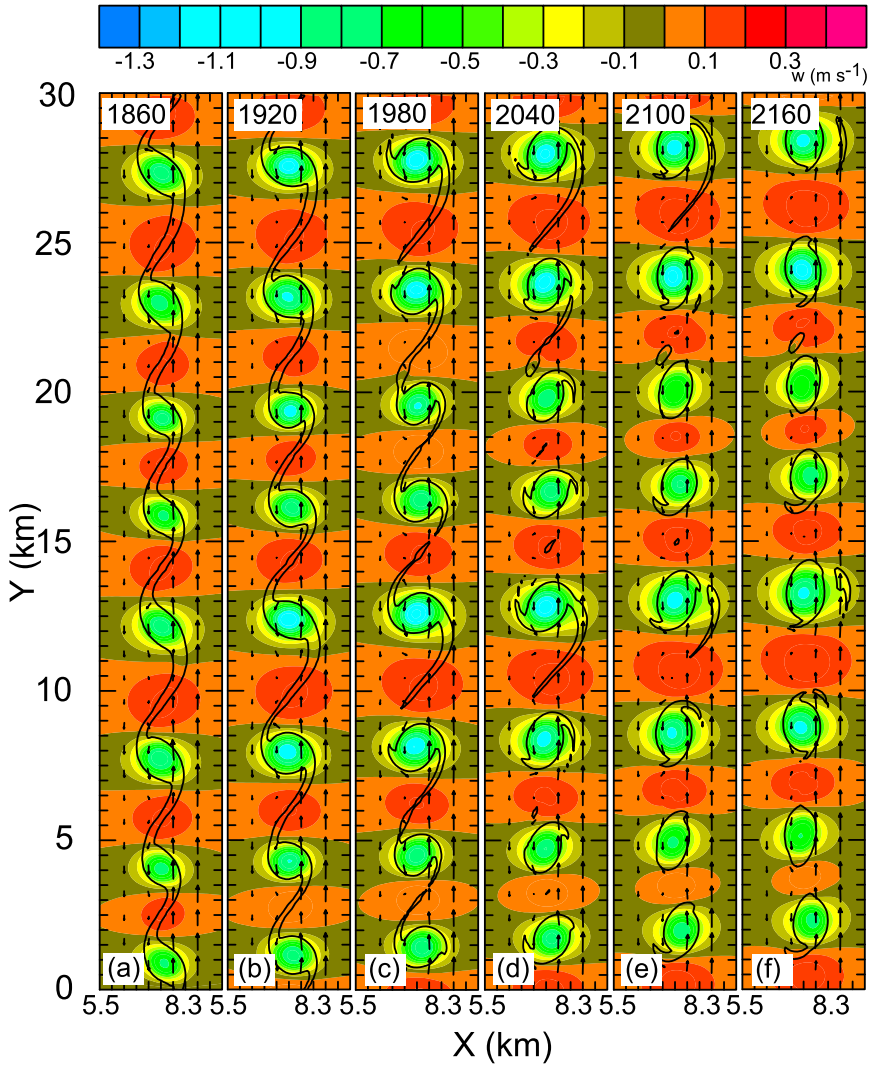

FIG. 15. As in Fig. 13, but for perturbation pressure in hPa (colors) and the $10 \times 10^{-3}\,s^{-1}$ vertical vorticity contour (black).

well up through rather large values of L. Small-amplitude wavelike features first become visible in the momentum fields after L achieves order 10%. The perturbations continue to grow exponentially at the same rate and peak wavenumber up through $L \sim 50\%$ or more. Thus, it appears that the predictions of linear theory may be extended into the nonlinear regime.

Even before visible waves can be seen in the simulations (about the time when the validity of linear theory weakens), spectral density estimates and growth rates can be computed. Therefore even from the beginning, the behavior of the simulations can be compared to linear theory with regard to the growth of small random perturbations.

Initially, there is a spinup period, where perturbations either do not grow exponentially or else are damped, followed by a period of exponential growth. This behavior is seen across all simulations and was also reported in a simulation of fluctuation growth along a frontogenetic oceanic front (McWilliams et al. 2009). After the spinup period the growth rates are essentially exponential as evidenced by the high linear correlation on semilog plots (not shown). As the width of the shear zone increases, the most-unstable wavelength also increases, remaining about 7.9 times the width of the shear zone, and this is independent of the magnitude of the shear across the zone. The growth rates of these maxima, however, are dependent on the magnitude of the vorticity in the layer and, thus, both the magnitude of the shear and the shear zone width. The larger the vorticity values, the larger the growth rates. Therefore, simulations with higher initial vorticity values have the emergence of wavelike structures and eventually discrete

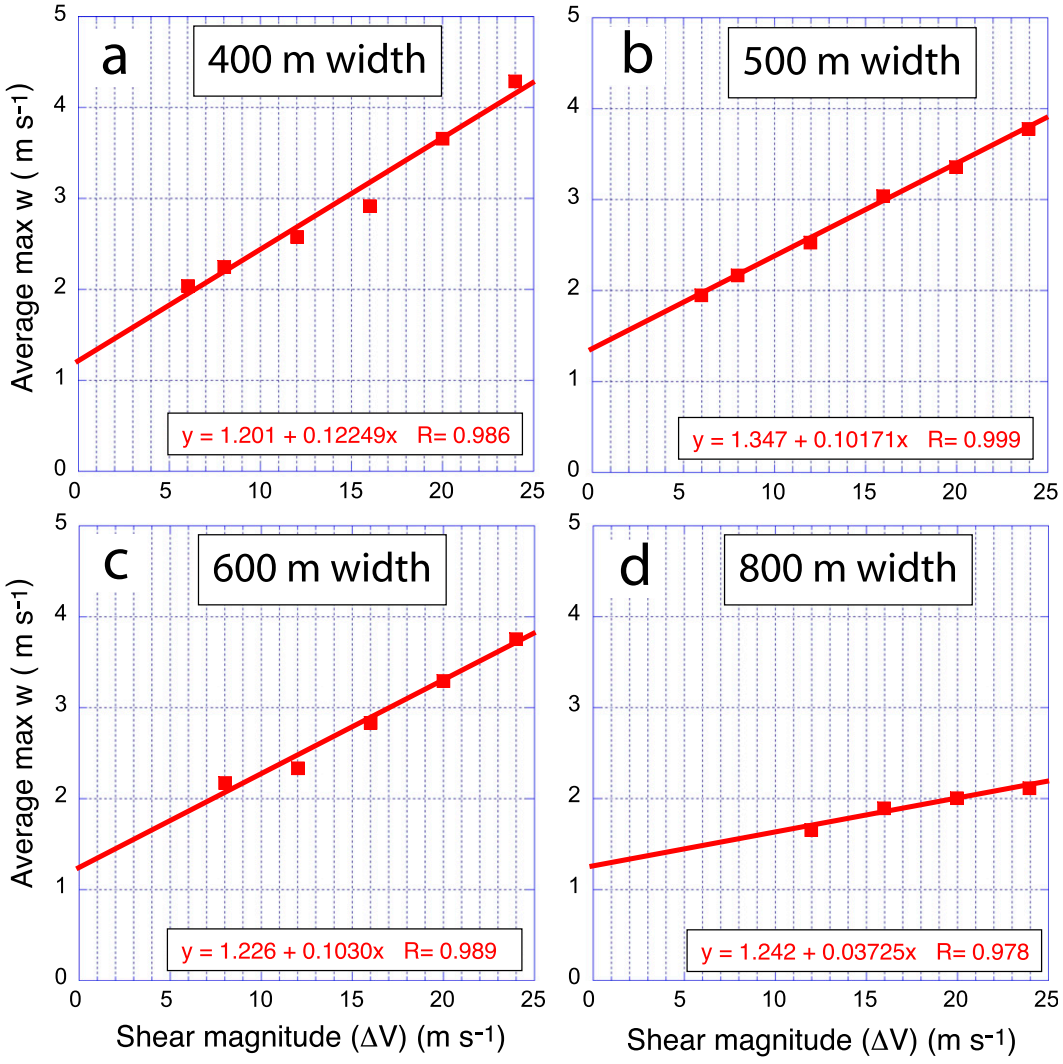

FIG. 16. As in Fig. 11, but for average maximum updraft (red squares) and the linear least squares fit (red line) for barotropic simulations.

vortices sooner than simulations with weaker initial vorticity values, since all simulations are initialized with the same random perturbation ($=0.01\,\mathrm{m\,s^{-1}}$).

Although the linear theory only holds while the growing perturbations are small (i.e., on the order of $0.1–1.0\,\mathrm{m\,s^{-1}}$ in the simulations), the discrete vortices that eventually form, albeit well into the nonlinear regime, possess wavelengths and spacings consistent with that predicted from linear theory. It therefore seems that linear theory can be extended to some degree into the nonlinear regime for these cases, or that the initial exponential growth "fixes" the structure of the later emerging vortices. These results agree with Harnik et al. (2014), who found that linear theory gave a good prediction of the structure into the nonlinear regime for a modified Rayleigh–Kuo problem. The results suggest in either way a degree of predictive value, in the sense that the spacing of discrete vortices can be determined prior to their emergence given an initial shear zone width. Also, if some estimate of the magnitude of the shear across the shear zone is known (hence vorticity), some estimate of the growth rates of the emerging vortices can also be estimated.

b. *Evolution of discrete vortices*

Once past the linear growth regime, discrete vortices develop nonlinearly. A common structure is seen across all barotropic simulations and is typified by the bt5m16s case shown. The nearly equally spaced vortices are elliptically shaped, grow in size, and are connected by thinning braid regions. As the vortices evolve, they rotate with a nearly constant angular velocity and eventually the braid regions wrap completely around the

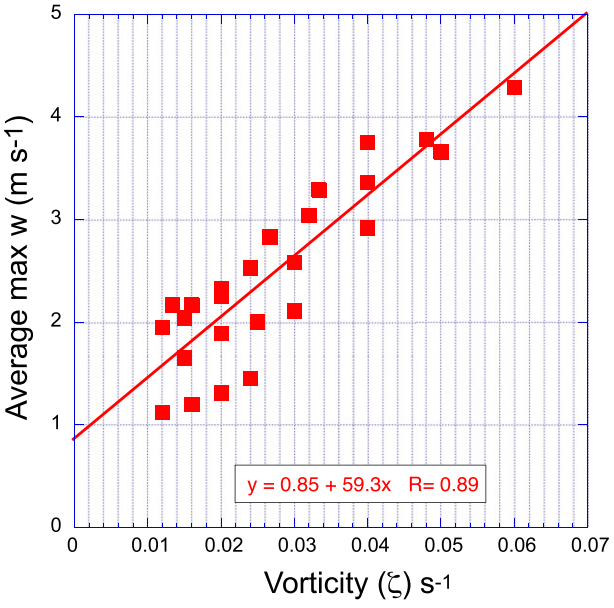

FIG. 17. Average maximum updraft for each barotropic simulation (red squares) and the linear least squares fit (red line) as a function of shear zone vorticity.

cores. This structure and evolution has been seen frequently in many observational and numerical studies (e.g., Freymuth 1966; Thorpe 1971; Brown and Roshko 1974; Winant and Browand 1974; Cantwell 1981; Corcos and Sherman 1984; Pozrikidis and Higdon 1985; Basak and Sarkar 2006; Guha et al. 2013). The evolving vortices also undergo nutation wherein the ratio of the major to minor axis length oscillates, another common feature of vortices under a variety of conditions (e.g., Kida 1981; Basak and Sarkar 2006; Guha et al. 2013). Eventually, the nonlinear interaction among the vortices leads to vortex pairing and mergers (e.g., Winant and Browand 1974; Basak and Sarkar 2006; Marquis et al. 2007).

c. *Vertical motions and cumulus formation in vortices*

Once the vortices have developed into discrete cores with connecting braids, relatively strong vertical motions fields also develop. To the authors' knowledge, no previous barotropic theoretical or numerical study has analyzed the velocity field along the direction of the vorticity within a shear zone (i.e., the vertical velocity component in the present study). Presumably, this is a result of the vast majority of the studies either being two dimensional (where no such velocity component exists) or that the orientation of the shear layer is such that the shear is in the vertical (i.e., the classic Kelvin–Helmholtz instability problem). In the present study the vertical velocity component is important, since simulations are interpreted as replicating real atmospheric boundaries and thus vertical motions can lead to CI and subsequent storm development. In the simulations, the stronger updrafts tend to occur where the braids attach to the cores. The strongest downdrafts tend to occur either along the braid regions or in the center of vortices. In the center of all vortices a local pressure perturbation minimum develops, and vortices have a tendency to develop central downdrafts. The tendency to form central downdrafts has also been seen in several observational studies (e.g., Markowski and Hannon 2006; Murphey et al. 2006; Marquis et al. 2007) and the modeling studies of Lee and Wilhemson (1997) and B12. Although not all vortices develop central downdrafts, those without central downdrafts also contain only weak updrafts.

Note that the lower boundary condition in the present study is free slip whereas in nature, there is interaction between the surface and the lower levels of vortices. A very shallow near-surface mixed shear layer that could be induced by surface drag forces would associate with vortex lines that are directed in toward the vortex center at the surface, subsequently turning upward very abruptly into the vertical vortex just above the surface. In observed atmospheric vortices, the vorticity is generally higher near the surface, leading to an increased downward directed perturbation pressure force. Therefore, real atmospheric vortices might be expected to have stronger central downdrafts. However, surface drag in atmospheric vortices are difficult to model robustly owing to the dependence on parameterization of the drag force and assumed (possibly highly variable) surface roughness as well as the very high near-surface spatial resolutions necessary to handle the large, shallow vertical shear layer.

Subjective analysis of several observational studies broadly conform to the updraft structure in the simulations—that is, generally strongest updrafts between or just north of vortex cores, weaker updrafts or downdrafts just south of vortex cores, and either the weakest updrafts or else downdrafts along the vortex axis (e.g., Wilson et al. 1992; Kawashima and Fujiyoshi 2005; Arnott et al. 2006; Marquis et al. 2007; B12; Campbell et al. 2014). This idealized vertical motion pattern when in the presence of sufficient moisture can produce cumuli away from the vortex core along the braid region (Fig. 20).

It has been shown that the average maximum updrafts that develop are highly correlated with the vorticity within the shear zone, with the stronger updrafts associated with higher vorticity values. Several previous studies have been reviewed to see if a similar correlation had been seen prior. Both observational and modeling studies were examined, and with the exception of one high-resolution modeling study (Lee and Wilhelmson 1997) there was only a small range in the strength of simulated or observed misocyclones. Most had vorticity

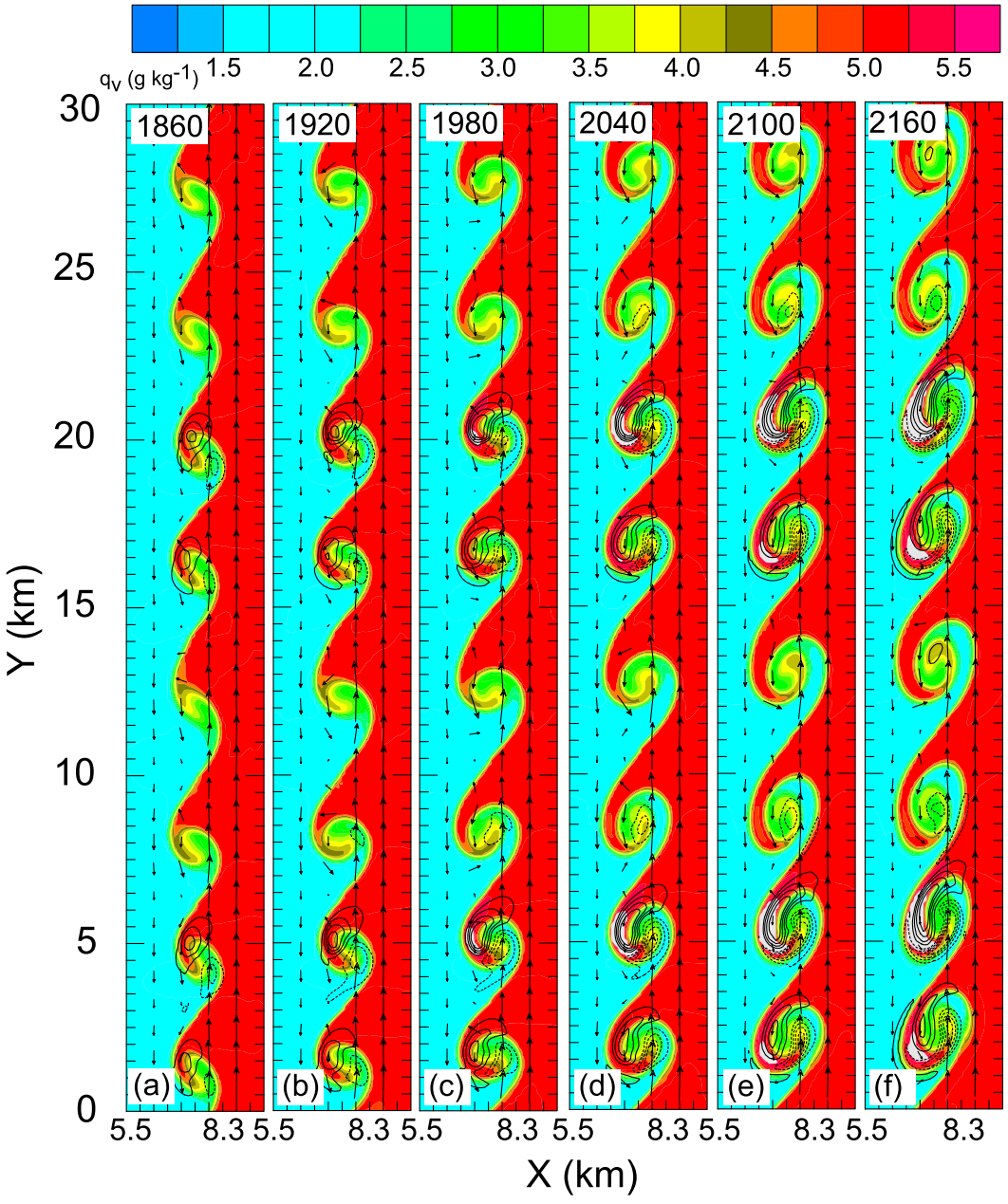

FIG. 18. As in Fig. 13, but for water vapor mixing ratio (color filled) at $z = 3$ km for the mbt5m16s case. The solid (dashed) black contours denote positive (negative) vertical velocity at 1 m s^{-1} intervals starting at 1 (-1) m s^{-1}. Also shown are the horizontal wind vectors (on the y axis is equivalent to 8 m s^{-1}). The white shaded regions denote cloud water mixing ratio >0.01 g kg^{-1}.

values around 8–10 $\times$ 10^{-3} s^{-1} and they were associated with vertical velocities of 2–4 m s^{-1} (Table 4). There is generally an increase in vertical velocity with increasing vorticity in these studies. Note that in the present study, the lowest initial shear zone vorticity values were 10 $\times$ 10^{-3} s^{-1} and the updrafts associated with these values were around 1–2 m s^{-1}. However, these were the average maximum vertical velocities in the domain; therefore, the simulation did have local updrafts greater than the average.

Although not all vortices have clouds and the extent of the clouds vary, it has been shown that the advection of the moisture fields and the vertical motions associated with vortices can force cumulus formation away from the vortex core (Fig. 20). Since the strongest updrafts are associated with the highest values of shear zone

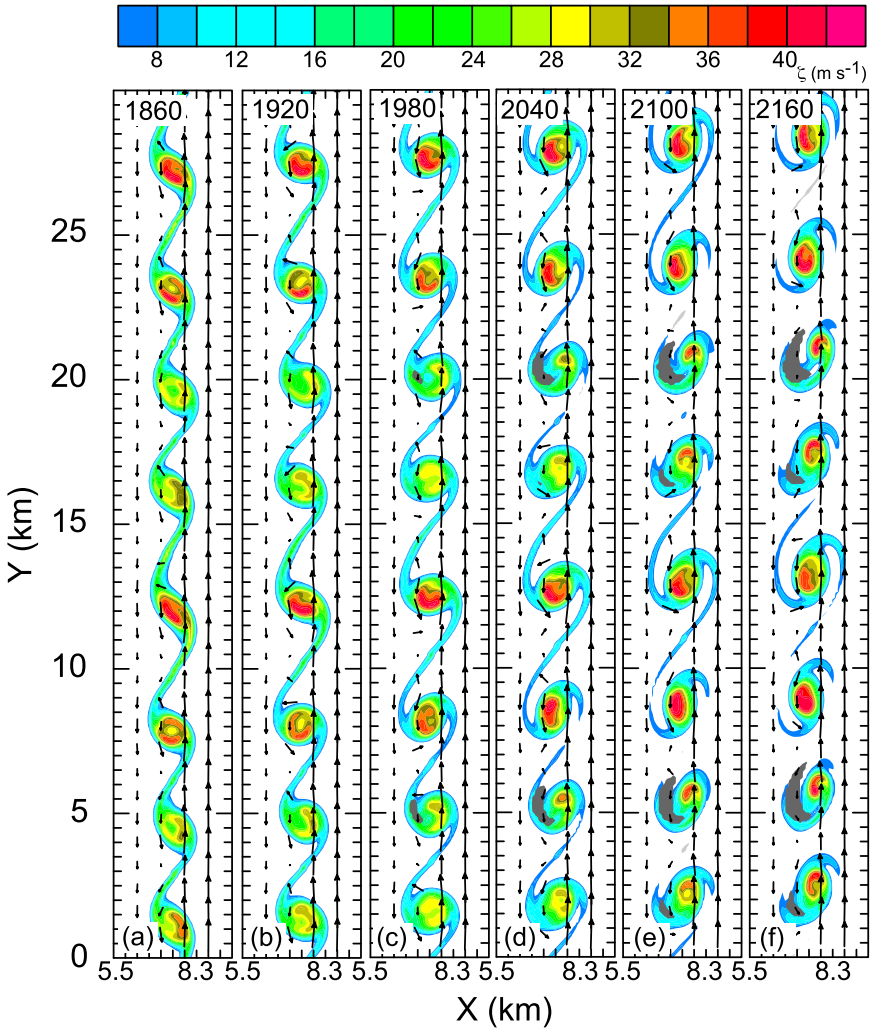

FIG. 19. As in Fig. 13, but for vertical vorticity at $z = 3$ km, with the solid gray shading denoting cloud water mixing ratio $>0.01\ \mathrm{g\,kg^{-1}}$. Also shown are the horizontal wind vectors (500 m on the y axis is equivalent to $8\ \mathrm{m\,s^{-1}}$).

vorticity, one would expect the largest and deepest developing clouds to also be associated with those shear zones with the highest vorticity values. Therefore, it is hypothesized that assessing the vorticity associated with a given shear zone (dryline, frontal zone, etc.) could yield some information about the potential for parcels to reach their LCLs and subsequent LFCs to trigger CI.

6. Conclusions

This study presents a series of idealized simulations that attempt to replicate shear zones typical of drylines and other near-surface boundaries to assess the possibility that the development of vortices with characteristic scales comparable to observed misocyclones is attributable to a purely HSI process. It is well known that near-surface boundaries often are associated with horizontal shear. These narrow shear zones can be organized on the synoptic scale associated with extratropical cyclones or on the mesoscale owing to varying surface processes. The series of 25 simulations are initialized with a north–south-oriented constant-vorticity shear zone, employ north–south periodic boundary conditions, and have varying magnitudes of shear and differing shear zone widths (corresponding to differing initial vorticity values). Additionally, four moist-barotropic simulations are rerun with moisture included under the constraint of horizontally homogeneous virtual potential temperature to assess preferred cumulus cloud formation areas.

Employing spectral estimates from the simulation output, comparison with linear theory consistently

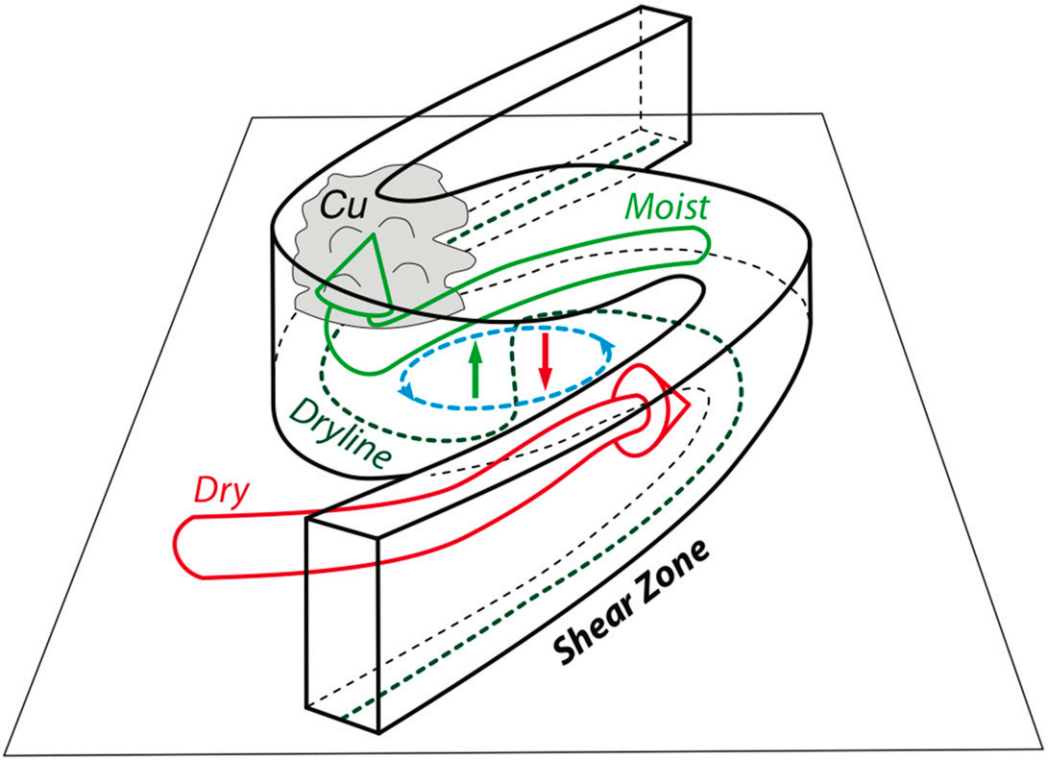

FIG. 20. Conceptual model of cumulus cloud formation relative to a shear-induced vortex along a dryline. The black contours denote the outer boundary of the deformed shear layer that contains vertical vorticity associated with the concentrated misocyclone and the weaker braids. The light green (red) 3D arrows denote the moist updraft (dry downdraft) to the northwest (southeast) of the vortex core. The blue contour denotes the highest values of vorticity near the surface. The dark green dashed curve represents the deformed surface dryline position. The vertical dark green (red) arrows denote moist upward (dry downward) motion near the vortex center. The gray shaded object represents a cumulus cloud.

reveals excellent agreement between the modeled and theoretical wavenumber (wavelength) of maximum growth. The most-unstable wavelength is approximately equal to 7.9 times the shear zone width. Excellent agreement between the predicted and simulated perturbation growth rate is also found. This growth rate is dependent on the layer vorticity as opposed to the shear zone width and shear magnitude independently, which should be expected on dimensional grounds. Thus, for these idealized simulations, linear HSI theory adequately explains the growth of small perturbations to form mature misocyclonic vortices at observed dryline scales.

A wave interaction theory (WIT) interpretation has been developed to better understand the physical mechanism by which vortices emerge from the initial shear zone. Within this framework, a shear zone consists of two or more density or vorticity discontinuities that can support two or more density or vorticity waves. The interaction of these waves can produce the instability if each interfacial wave amplifies the other. This theoretical interpretation predicts the initial wavelength and

TABLE 4. List of several previous studies that discussed misocyclones, including their description and their values of maximum vertical vorticity and maximum updraft.

Study	Description	Maximum vorticity ($\times 10^{-3}$ s^{-1})	Maximum updraft (m s^{-1})
Kawashima and Fujiyoshi (2005)	Radar observations	10	3–4
Lee and Wilhelmson (1997)	100-m-resolution simulation	70–80	8–9
Arnott et al. (2006)	Radar observations	8	2–3
Wilson et al. (1992)	1-km-resolution simulation	10	3–4
Campbell et al. (2014)	1-km-resolution simulation	8	2
Kawashima (2011)	500-m-resolution simulation	10	3–4
Buban et al. (2007)	Radar observations	8	3

phase shift of the corresponding most-unstable mode predicted by linear theory. The results of the calculated initial phase shifts and wavelengths are consistent with the WIT interpretation of the horizontal shearing instability.

Although linear HSI theory is only strictly valid for perturbations that are small compared to the background flow (i.e., <10% of the shear magnitude), the simulations nevertheless demonstrate that the unstable perturbations continuously intensify from the linear into the nonlinear flow regime. The simulated vortices resulting from barotropic shearing instability are persistently spaced near the predicted wavenumber (wavelength) of maximum growth, and shear zones with larger growth rates develop discrete vortices faster than those with smaller growth rates. Linear HSI theory appears to extend into the nonlinear regime in the sense that the fastest-growing HSI mode continues to grow fastest and eventually emerges as the dominant mode well within the nonlinear regime. Thus, applying linear theory appears to facilitate the prediction of the characteristic spacing, size, and growth rate parameters of mature vortices with structures similar to observed atmospheric vortices.

The simulated vortices all become elliptically shaped as they grow in size and rotate counterclockwise with a nearly constant angular velocity. The simulated vortices are also connected by thinning braid regions, develop a pressure minimum in the vortex core, and tend to develop a central downdraft. The vertical motion fields generally feature the weakest updrafts or downdrafts in the vortex core, with stronger updrafts along the braids or edges of the vortex core. This common structure and evolution of the simulated vortices has been seen frequently in many previous observational and numerical studies.

The moist-barotropic simulations have been conducted to determine preferred regions of cumulus formation relative to the ambient shear zone and misocyclones. In all moist simulations, cumuli develop in the region where a core connects to a braid. This region contains the strongest updrafts in collocation with regions of larger water vapor mixing ratio values in a deeper layer, with the stronger updrafts producing the largest and deepest clouds. It is also found that the average local maximum in updraft increases with increasing vorticity. Also, updraft spacing decreases with decreasing shear zone width. Thus, it is hypothesized that narrower shear zones with and shear zones with higher initial vertical vorticity values may be expected to develop either more or larger cumuli. It is also hypothesized that shear zones possessing an enhanced conditional probability of deep cumulus formation may associate with higher probability of CI.

Acknowledgments. The lead author gratefully acknowledges helpful discussions with committee members Drs. Michael Biggerstaff, Alan Shapiro, Evgeni Fedorovich, Louis Wicker, S. Lakshmivarahan, and his advisor (CLZ) during the preparation of his Ph.D. dissertation at the University of Oklahoma (a portion of which the present study reports). Edward Mansell and Alison Silveira are also gratefully acknowledged for assistance with COMMAS model code. Major funding for the current project was provided under National Science Foundation Grants AGS-0130316, AGS-0638572, and AGS-1063537 and by the NOAA/National Severe Storms Laboratory. Funding was also provided by NOAA/Office of Oceanic and Atmospheric Research under NOAA-University of Oklahoma Cooperative Agreement NA11OAR4320072, U.S. Department of Commerce.

REFERENCES

Arnott, N. R., Y. P. Richardson, J. M. Wurman, and E. M. Rasmussen, 2006: Relationship between a weakening cold front, misocyclones, and cloud development on 10 June 2002 during IHOP. *Mon. Wea. Rev.*, **134**, 311–335, doi:10.1175/MWR3065.1.

Atkins, N. T., R. M. Wakimoto, and T. M. Weckwerth, 1995: Observations of the sea-breeze front during CaPE. Part II: Dual-Doppler and aircraft analysis. *Mon. Wea. Rev.*, **123**, 944–969, doi:10.1175/1520-0493(1995)123<0944:OOTSBF>2.0.CO;2.

Balsa, T. F., 1987: On the spatial instability of piecewise linear free shear layers. *J. Fluid Mech.*, **174**, 553–563, doi:10.1017/S0022112087000247.

Basak, S., and S. Sarkar, 2006: Dynamics of a stratified shear layer with horizontal shear. *J. Fluid Mech.*, **568**, 19–54, doi:10.1017/S0022112006001686.

Betchov, R., and A. Szewczyk, 1963: Stability of a shear layer between parallel streams. *Phys. Fluids*, **6**, 1391–1396, doi:10.1063/1.1710959.

Brown, G. L., and A. Roshko, 1974: On density effects and large structures in turbulent mixing layers. *J. Fluid Mech.*, **64**, 775–816, doi:10.1017/S002211207400190X.

Buban, M. S., 2014: The formation of small-scale atmospheric vortices via horizontal shearing instability. Ph.D. dissertation, University of Oklahoma, 215 pp. [Available online at http://hdl.handle.net/11244/13870.]

——, C. L. Ziegler, E. N. Rasmussen, and Y. P. Richardson, 2007: The dryline on 22 May 2002 during IHOP: Ground-radar and in situ data analyses of the dryline and boundary layer evolution. *Mon. Wea. Rev.*, **135**, 2473–2505, doi:10.1175/MWR3453.1.

——, ——, E. R. Mansell, and Y. P. Richardson, 2012: Simulation of dryline misovortex dynamics and cumulus formation. *Mon. Wea. Rev.*, **140**, 3525–3551, doi:10.1175/MWR-D-11-00189.1.

Campbell, P. C., B. Geerts, and P. T. Bergmaier, 2014: A dryline in southeast Wyoming. Part I: Multiscale analysis using observations and modeling on 22 June 2010. *Mon. Wea. Rev.*, **142**, 268–289, doi:10.1175/MWR-D-13-00049.1.

Cantwell, B. J., 1981: Organized motion in turbulent flow. *Annu. Rev. Fluid Mech.*, **13**, 457–515, doi:10.1146/annurev.fl.13.010181.002325.

Carpenter, J. R., E. W. Tedford, E. Heifetz, and G. A. Lawrence, 2013: Instability in stratified shear flow: Review of a physical

interpretation based on interacting waves. *Appl. Mech. Rev.*, **64**, 060801, doi:10.1115/1.4007909.

Coniglio, M. C., D. J. Stensrud, and L. J. Wicker, 2006: Effects of upper-level shear on the structure and maintenance of strong quasi-linear mesoscale convective systems. *J. Atmos. Sci.*, **63**, 1231–1252, doi:10.1175/JAS3681.1.

Corcos, G. M., and F. S. Sherman, 1984: The mixing layer: Deterministic models of a turbulent flow. Part 1. Introduction and the two-dimensional flow. *J. Fluid Mech.*, **139**, 29–65, doi:10.1017/S0022112084000252.

Crook, N. A., T. L. Clark, and M. W. Moncrieff, 1991: The Denver cyclone. Part II: Interaction with the convective boundary layer. *J. Atmos. Sci.*, **48**, 2109–2126, doi:10.1175/1520-0469(1991)048<2109:TDCPII>2.0.CO;2.

Drazin, P. G., and L. N. Howard, 1962: The instability to long waves of unbounded parallel inviscid flow. *J. Fluid Mech.*, **14**, 257–283, doi:10.1017/S0022112062001238.

Esch, R. E., 1957: The instability of a shear layer between two parallel streams. *J. Fluid Mech.*, **3**, 289–303, doi:10.1017/S002211205700066X.

Farrell, B. F., 1984: Modal and non-modal baroclinic waves. *J. Atmos. Sci.*, **41**, 668–673, doi:10.1175/1520-0469(1984)041<0668:MANMBW>2.0.CO;2.

Freymuth, P., 1966: On the transition in a separated laminar boundary layer. *J. Fluid Mech.*, **25**, 683–704, doi:10.1017/S002211206600034X.

Guha, A., M. Rahmani, and G. A. Lawrence, 2013: Evolution of a barotropic shear layer into elliptical vortices. *Phys. Rev.*, **87E**, 013020, doi:10.1103/PhysRevE.87.013020.

Harnik, N., D. G. Dritschel, and E. Heifetz, 2014: On the equilibrium of asymmetric barotropic instability. *Quart. J. Roy. Meteor. Soc.*, **140**, 2444–2464, doi:10.1002/qj.2310.

Hazel, P., 1972: Numerical studies of the stability of inviscid stratified shear flows. *J. Fluid Mech.*, **51**, 39–61, doi:10.1017/S0022112072001065.

Heifetz, E., and J. Methven, 2005: Relating optimal growth to counter-propogating Rossby waves in shear instability. *Phys. Fluids*, **17**, 064107, doi:10.1063/1.1937064.

——, C. H. Bishop, and P. Alpert, 1999: Counter-propagating Rossby waves in the barotropic Rayleigh model of shear instability. *Quart. J. Roy. Meteor. Soc.*, **125**, 2835–2853, doi:10.1256/smsqj.56003.

Jenkins, G. M., and D. G. Watts, 1969: *Spectral Analysis and Its Applications*. Holden-Day, 525 pp.

Kanak, K. M., 2008: Vortical structures in convective boundary layers and implications for the initiation of deep convection. *24th Conf. on Severe Local Storms*, Savannah, GA, Amer. Meteor. Soc., 18.3. [Available online at https://ams.confex.com/ams/24SLS/techprogram/paper_142080.htm.]

Kawashima, M., 2011: Numerical study of horizontal shear instability waves along narrow cold frontal rainbands. *J. Atmos. Sci.*, **68**, 878–903, doi:10.1175/2010JAS3599.1.

——, and Y. Fujiyoshi, 2005: Shear instability wave along a snowband: Instability structure, evolution, and energetics derived from dual-Doppler radar data. *J. Atmos. Sci.*, **62**, 351–370, doi:10.1175/JAS-3392.1.

Kida, S., 1981: Motion of an elliptic vortex in a uniform shear flow. *J. Phys. Soc. Japan*, **50**, 3517–3520, doi:10.1143/JPSJ.50.3517.

Lee, B. D., and R. B. Wilhelmson, 1997: The numerical simulation of non-supercell tornadogenesis. Part I: Initiation and evolution of pretornadic misocyclone circulations along a dry outflow boundary. *J. Atmos. Sci.*, **54**, 32–60, doi:10.1175/1520-0469(1997)054<0032:TNSONS>2.0.CO;2.

——, C. A. Finley, and R. B. Wilhelmson, 2000: Simulating deep convection initiation by misocyclones. Preprints, *20th Conf. on Severe Local Storms*, Orlando, FL, Amer. Meteor. Soc., P2.3. [Available online at https://ams.confex.com/ams/Sept2000/techprogram/paper_16291.htm.]

Lessen, M., 1950: On stability of free laminar boundary layer between parallel streams. NACA Tech. Rep. 979, 571–579. [Available online at http://digital.library.unt.edu/ark:/67531/metadc60317/.]

Mansell, E. R., C. L. Ziegler, and E. C. Bruning, 2010: Simulated electrification of a small thunderstorm with two-moment bulk microphysics. *J. Atmos. Sci.*, **67**, 171–194, doi:10.1175/2009JAS2965.1.

Markowski, P., and C. Hannon, 2006: Multiple-Doppler radar observations of the evolution of vorticity extrema in a convective boundary layer. *Mon. Wea. Rev.*, **134**, 355–374, doi:10.1175/MWR3060.1.

Marquis, J., Y. P. Richardson, and J. M. Wurman, 2007: Kinematic observations of misocyclones along boundaries during IHOP. *Mon. Wea. Rev.*, **135**, 1749–1768, doi:10.1175/MWR3367.1.

McWilliams, J. C., M. J. Molemaker, and E. I. Olafsdottir, 2009: Linear fluctuation growth during frontogenesis. *J. Phys. Oceanogr.*, **39**, 3111–3129, doi:10.1175/2009JPO4186.1.

Michalke, A., 1965: On spatially growing disturbances in an inviscid shear layer. *J. Fluid Mech.*, **23**, 521–544, doi:10.1017/S0022112065001520.

Miles, J. W., 1961: On the stability of heterogeneous shear flows. *J. Fluid Mech.*, **10**, 496–508, doi:10.1017/S0022112061000305.

Murphey, H. V., R. M. Wakimoto, C. Flamant, and D. E. Kingsmill, 2006: Dryline on 19 June 2002 during IHOP. Part I: Airborne Doppler and LEANDRE II analyses of the thin line structure and convection initiation. *Mon. Wea. Rev.*, **134**, 406–430, doi:10.1175/MWR3063.1.

Pedlosky, J., 1987: *Geophysical Fluid Dynamics*. Springer-Verlag, 710 pp.

Pietrycha, A. E., and E. N. Rasmussen, 2004: Finescale surface observations of the dryline: A mobile mesonet perspective. *Wea. Forecasting*, **19**, 1075–1088, doi:10.1175/819.1.

Pozrikidis, C., and J. J. L. Higdon, 1985: Nonlinear Kelvin–Helmholtz instability of a finite vortex layer. *J. Fluid Mech.*, **157**, 225–263, doi:10.1017/S0022112085002361.

Rayleigh, L., 1880: On the stability, or instability, of certain fluid motions. *Proc. London Math. Soc.*, **11**, 57–70, doi:10.1112/plms/s1-11.1.57.

Rosenhead, L., 1931: The formation of vortices from a surface of discontinuity. *Proc. Roy. Soc. London*, **134**, 170–192, doi:10.1098/rspa.1931.0189.

Sato, H., 1960: The stability and transition of a two-dimensional jet. *J. Fluid Mech.*, **7**, 53–80, doi:10.1017/S0022112060000049.

Schade, H., and A. Michalke, 1962: Zur Entstehung von Wirbeln in einer freien Grenzschicht. *Z. Flugwiss.*, **10**, 147–154.

Scotti, R. S., and G. M. Corcos, 1972: An experiment on the stability of small disturbances in a stratified free shear layer. *J. Fluid Mech.*, **52**, 499–528, doi:10.1017/S0022112072001569.

Thorpe, S. A., 1971: Experiments on the instability of stratified shear flows: Miscible fluids. *J. Fluid Mech.*, **46**, 299–319, doi:10.1017/S0022112071000557.

Trefethen, L. N., A. E. Trefethen, S. C. Reddy, and T. A. Driscoll, 1993: Hydrodynamic stability without eigenvalues. *Science*, **261**, 578–584, doi:10.1126/science.261.5121.578.

Vitoshkin, H., E. Heifetz, A. Yu. Gelfgat, and H. Harnik, 2012: On the role of vortex stretching in energy optimal growth of three-dimensional perturbations on plane parallel shear flows. *J. Fluid Mech.*, **707**, 369–380, doi:10.1017/jfm.2012.285.

Wakimoto, R. M., and H. V. Murphey, 2009: Analysis of a dryline during IHOP: Implications for convection initiation. *Mon. Wea. Rev.*, **137**, 912–936, doi:10.1175/2008MWR2584.1.

Wicker, L. J., and R. B. Wilhelmson, 1995: Simulation and analysis of tornado development and decay within a three-dimensional supercell thunderstorm. *J. Atmos. Sci.*, **52**, 2675–2703, doi:10.1175/1520-0469(1995)052<2675:SAAOTD>2.0.CO;2.

——, and W. Skamarock, 2002: Time-splitting methods for elastic models using forward time schemes. *Mon. Wea. Rev.*, **130**, 2088–2097, doi:10.1175/1520-0493(2002)130<2088:TSMFEM>2.0.CO;2.

Wilson, J. W., G. B. Foote, N. A. Crook, J. C. Frankhauser, C. G. Wade, J. D. Tuttle, C. K. Mueller, and S. K. Kruger, 1992: The role of boundary-layer convergence zones and horizontal rolls in the initiation of thunderstorms: A case study. *Mon. Wea. Rev.*, **120**, 1785–1815, doi:10.1175/1520-0493(1992)120<1785:TROBLC>2.0.CO;2.

Winant, C. D., and F. K. Browand, 1974: Vortex pairing: The mechanism of turbulent mixing-layer growth at moderate Reynolds number. *J. Fluid Mech.*, **63**, 237–255, doi:10.1017/S0022112074001121.